

Nuclear Multifragmentation and Phase Transition for hot nuclei

B. Borderie*, M. F. Rivet,

Institut de Physique Nucléaire, CNRS/IN2P3, Université Paris-Sud 11, F-91406 Orsay Cedex, France

Abstract

That review article is focused on the tremendous progresses realized during the last fifteen years in the understanding of multifragmentation and its relationship to the liquid-gas phase diagram of nuclei and nuclear matter. The explosion of the whole nucleus, early predicted by Niels Bohr [1], is a very complex and rich subject which continues to fascinate nuclear physicists as well as theoreticians who extend the thermodynamics of phase transitions to finite systems.

Key words: Multifragmentation

PACS: 25.70.-z, 25.70.Pq, 24.60.Ky, 64.60.-i

Contents

1	Introduction	3
2	A general survey	4
2.1	Nuclear matter at subnormal density and phase transition	4
2.2	Evolution of decay mechanisms: from evaporation to vaporization	6
3	Experimental event sorting	9
3.1	Impact parameter selectors	10
3.2	Topology selectors	13
3.3	Multivariate analysis techniques	14
3.4	Cross sections	14

* Corresponding author - borderie@ipno.in2p3.fr
Email address: rivet@ipno.in2p3.fr (M. F. Rivet).

3.5	Conclusion	15
4	Fragment properties	15
4.1	Multiplicities	16
4.2	Z_{bound}^f and charge distributions in central collisions	19
4.3	Energy distributions - expansion	20
4.4	The specific role of the largest fragment	22
4.5	Summary on size effects	24
5	Theoretical descriptions of nuclear fragmentation and comparison to data	24
5.1	Statistical ensembles and models	25
5.2	Statistical descriptions of multifragmentation	26
5.3	Dynamical descriptions of multifragmentation	27
5.4	The link between dynamical and statistical descriptions	33
6	Calorimetry and thermometry	34
6.1	Calorimetry	34
6.2	Temperature measurements	37
6.3	Caloric curves	39
7	Freeze-out properties	40
7.1	Fragment velocity correlations and event topology at freeze-out	40
7.2	Fragment-particle correlations and fragment excitation at freeze-out	43
7.3	Break-up densities and freeze-out volumes	44
8	Finite systems and phase transitions	46
8.1	Dynamics and spinodal instability	46
8.2	Spinodal instability and Thermostatistics	50
8.3	Scaling and fluctuations for fragment sizes	56
9	Coherent experimental signals of phase transition	60

1 Introduction

The nuclear multifragmentation phenomenon was predicted and studied since the early 80's. It is however only with the advent of powerful 4π detectors [2] that real advances were made. Such arrays allow the detection of a large amount of the many fragments and light particles produced in nuclear collisions at intermediate and high energies. Indeed it now appears that further progresses are linked to the knowledge of many observables and the possibility to study correlations inside the multifragment events. This paper is a snapshot of what is known at the present time, making use of a large panel of the available data from heavy-ion collisions at intermediate energies, and from hadron-nucleus collisions. A comparison between fragmentation properties of quasi-projectiles formed in semi-peripheral collisions and of "fused" systems produced in the more violent ones will be particularly developed. The formation of the fragmenting systems (or sources) in the course of nuclear collisions makes it necessary to model the collisions and several transport codes have been developed for two decades [3, 4], which account for many properties experimentally observed. On the other hand statistical descriptions based on phase space occupation also account well for the static properties (partitions) of multifragmenting systems. The connection between both descriptions will be discussed. The Equation of State describing nuclear matter, similar to the van der Waals equation for classical fluids, foresees the existence of a liquid-gas type phase transition; multifragmentation was long-assimilated to this transition (or to a "liquid-fog" transition [5]). Nuclear physicists are however dealing with finite systems - nuclei feeling nuclear and Coulomb forces - and not with infinite nuclear matter. Following the concepts of statistical physics, a new definition of phase transitions for such systems was recently proposed, showing that specific phase transition signatures could be expected. Different and coherent signals of phase transition have indeed been evidenced in a few cases.

After a general survey of the multifragmentation phenomenon in section 2, the necessity of sorting events and the different ways to proceed are presented in section 3. The properties of the emitted fragments are detailed in section 4. Section 5 introduces statistical and dynamical models whose results are commonly compared to experimental data. The reconstruction of the multifragmenting systems connected with calorimetric and thermometric measurements (section 6) is followed by a study of the properties of these systems at the freeze-out stage in section 7. Finally the view of multifragmentation in terms of the phase transition of a finite system and the experimental signatures evidencing the transition are developed in sections 8 and 9.

2 A general survey

One can come to the multifragmentation concept and its relation to a phase transition from two different starting points. Firstly by using kinetic models which show that nucleus-nucleus collisions at intermediate energies produce matter at subnormal density which breaks and where a phase transition is predicted to occur; it is a pure theoretical starting point. The other one consists in studying both experimentally and theoretically the evolution of decay mechanisms with increasing excitation energy.

2.1 Nuclear matter at subnormal density and phase transition

2.1.1 The nuclear liquid-gas phase transition

Nuclear matter is an idealized macroscopic system with an equal number of neutrons and protons. It interacts via nuclear forces, and Coulomb forces are ignored due to its size. Its density ρ is spatially uniform. The nucleon-nucleon interaction is constituted by two components according to their radial interdistance : a very short-range repulsive part which takes into account the compressibility of the medium and a long-range attractive part. Changed by five orders of magnitude the nuclear interaction is similar to van der Waals forces acting in molecular medium. In a sense the phase transition in nuclear matter resembles the liquid-gas phase transition in classical fluids. However, as compared to classical fluids the main difference comes from the gas composition: for nuclear matter the gas phase is predicted to be composed not only of single nucleons, neutrons and protons, but also of complex particles and fragments depending on temperature conditions [6, 7].

A set of isotherms for an equation of state (pressure versus density) corresponding to nuclear forces (Skyrme effective interaction and finite temperature Hartree-Fock theory [8]) is shown in figure 1. It exhibits the maximum-minimum structure typical of van der Waals equation of state. Depending on the effective interaction chosen and on the model [8, 9, 10, 11], the nuclear equation of state exhibits a critical point at $\rho_c \approx -0.3-0.4\rho_0$ and $T_c \approx 16-18$ MeV. ρ_0 and V_0 refer to normal density/volume. The region below the dotted line in figure 1 corresponds to a domain of negative compressibility: at constant temperature an increase of density is associated to a decrease of pressure. Therefore in this region a single homogeneous phase is unstable and the system breaks into a liquid phase and a gas phase in equilibrium. It is the so called spinodal region, and spinodal instability corresponds to the breaking into the two phases. Such instability has been proposed, for a long time, as a possible mechanism responsible for multifragmentation [12, 13, 14]. It will be discussed in section 8. The spinodal region constitutes the major part of

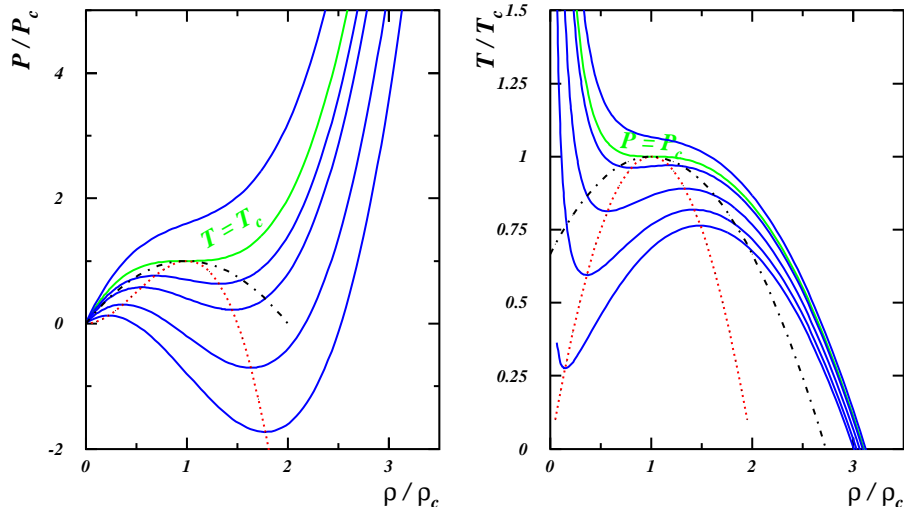


Fig. 1. Equation of state relating the pressure (left) or the temperature (right) and the density (normalised to critical values) in nuclear matter. The curves represent isotherms (left) and isobars (right). The dashed-dotted lines are the coexistence lines and the dotted lines the spinodal lines (from [15]).

the coexistence region (dashed-dotted line in figure 1) which also contains two metastable regions: one at density below ρ_c for the nucleation of drops and one above ρ_c for the nucleation of bubbles (cavitation).

2.1.2 From nuclear matter to hot nuclei

Evidently the hot piece of nuclear matter produced in any nuclear collision has at more a few hundreds nucleons and so is not adequately described by the properties of infinite nuclear matter; surface and Coulomb effects can not be ignored. These effects have been evaluated and lead to a sizeable reduction of the critical temperature [8, 9, 16]. Finite size effects have been found to reduce the temperature by 2-6 MeV depending on the size of nuclei while the Coulomb force is responsible for a further reduction of 1-3 MeV. However large reductions due to small sizes are associated with small reductions from Coulomb. Consequently, in the range $A=50-400$ a total reduction of about 7 MeV is calculated leading to a “critical” temperature of about 10 MeV for nuclei or hot pieces of nuclear matter produced in collisions between very heavy nuclei. The authors of reference [9] indicate that, due to some approximations, the derived values can be regarded as upper limits. Finally we can recall that, in infinite nuclear matter, the binding energy per particle is 16 MeV whereas it is about 8 MeV in a finite nucleus. Clearly these values well compare with the T_c values for infinite nuclear matter and nuclei just discussed.

2.2 *Evolution of decay mechanisms: from evaporation to vaporization*

2.2.1 *Evaporation*

The behaviour of nuclei at excitation energies around 1 MeV/nucleon has been extensively studied and rather well understood using statistical models [17]. The theoretical treatment of particle emission involves the estimation of microstate densities defined for equilibrium states. Such a treatment is justified only when there is enough time between successive emissions for the relaxation of the emitting nucleus to a new equilibrium state. At such excitation energies the density stays very close to normal density of cold nuclear matter and the earliest evaporation model rests on the basic idea: an emitted particle can be considered as originally situated somewhere on the surface of the emitting nucleus with a randomly directed velocity, it is why we use the term evaporation. Moreover particles are emitted sequentially and independently without any correlation. Note that in this excitation energy domain fission is also a deexcitation mechanism and can compete with evaporation.

2.2.2 *The multifragmentation domain*

At excitation energies comparable with the binding energy of nuclei a copious emission of particles and fragments is experimentally observed and the name “multifragmentation” was introduced. A first attempt to connect multifragmentation to a possible phase transition is to derive the excitation energy domain where this type of deexcitation is experimentally observed. Figure 2 displays, for different reactions, the evolution of the average fragment multiplicity, normalized to the size of the multifragmenting system, as a function of the excitation energy per nucleon deposited into the system. All points fall on a single bell shape curve. The onset of multifragmentation takes place for excitation energies around 3 MeV/nucleon and the maximum for fragment production is found around 9 MeV/nucleon, i.e. close to the binding energy of nuclei. At higher excitation energy, due to the opening of the vaporization channel, the fragment production reduces. On the other hand, average time intervals between successive emissions have been estimated by analysing space-time correlations between fragments, taking advantage of proximity effects induced by Coulomb repulsion. Figure 3 displays those average time intervals measured as a function of excitation energy deposited into the emitting system. A strong decrease of measured times with the increase of excitation energy is observed up to around 5 MeV/nucleon. Then a saturation appears around 50-100 fm/c which reflects the limit of sensitivity of the method. For such short times fragments can be considered as emitted quasi simultaneously and fragment emissions can not be treated independently. Note that, correlatively, sequential statistical models fail in reproducing the observed emission

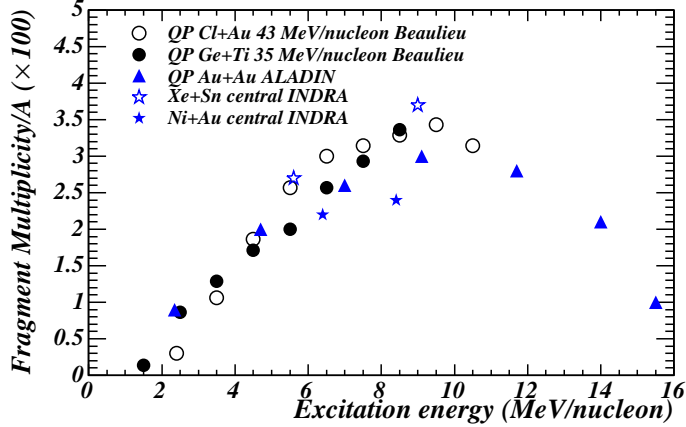


Fig. 2. Average fragment multiplicity (normalized to the number of incident nucleons) as a function of the excitation energy per nucleon (data from [18, 19, 20, 21]).

characteristics [22].

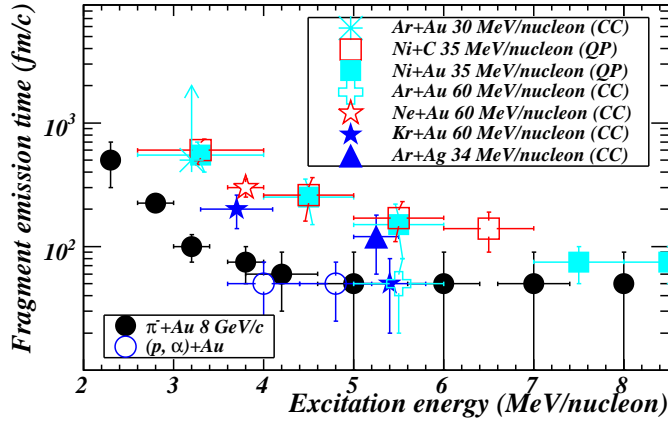


Fig. 3. Average fragment emission time as a function of the excitation energy per nucleon (data from [23, 24, 25, 26, 27, 28, 29, 30]. CC stands for central collisions, QP for quasi-projectile sources).

2.2.3 Vaporization and identification of a gas phase

At excitation energies around 10 MeV/nucleon, first experimental indications for the onset of vaporization (disintegration into light particles with $Z \leq 2$) were reported in references [31, 32, 33, 34, 35]. Moreover a gas phase was identified by comparison with a model by studying the deexcitation properties of vaporized quasi-projectiles produced in $^{36}\text{Ar}+^{58}\text{Ni}$ reactions [36]. Chemical composition and average kinetic energies of the different particles are well reproduced by a quantum statistical model (grandcanonical approach) describing a real gas of fermions and bosons in thermal and chemical equilibrium. The evolution with excitation energy of the composition of vaporized quasi-projectiles is shown in figure 4. Nucleon production increases with excitation

energy whereas emission of alpha particles, dominant at lower excitation energies, strongly decreases. The regular behaviour observed is a strong indication that a rapid change of phase does not occur in the considered excitation energy range. Note that an excluded volume correction due to finite particle size [37] (van der Waals-like behaviour) was found decisive to obtain the observed agreement. In the model, the experimental range in excitation energy

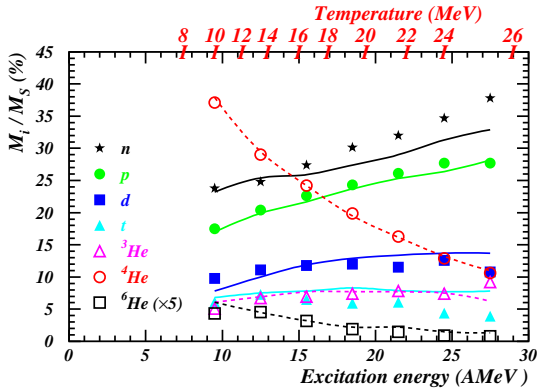


Fig. 4. Composition of vaporized quasi-projectiles, formed in 95 MeV/nucleon $^{36}\text{Ar}+^{58}\text{Ni}$ collisions, as a function of their excitation energy per nucleon. Symbols are for data while the lines (dashed for He isotopes) are the results of the model. The temperature values used in the model are also given. (from [36]).

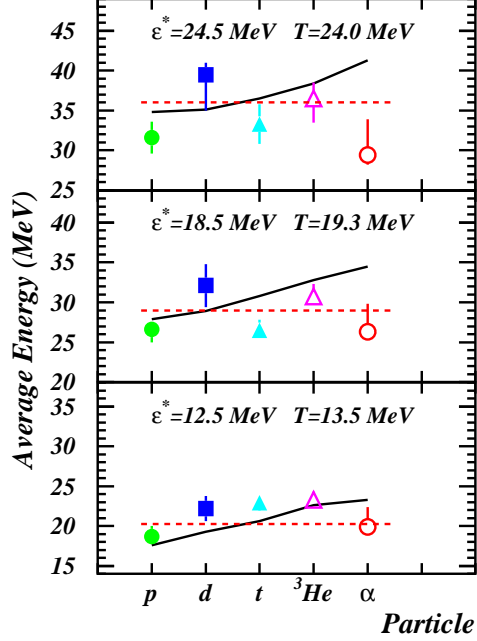


Fig. 5. Average kinetic energies of particles emitted by vaporized quasi-projectiles at different excitation energies and formed in 95 MeV/nucleon $^{36}\text{Ar}+^{58}\text{Ni}$ collisions. Symbols are for data while full lines are the results of the model. The dashed lines refer to average kinetic energies of particles expected for an ideal gas ($3T/2$) at temperatures derived from the model. (from [36]).

per nucleon of the source (9.5 to 27.5 MeV) was covered by varying the temperature from 10 to 25 MeV and the only free parameter, the free volume, was fixed at $3V_0$ in order to reproduce the experimental ratio between the proton and alpha yields at 18.5 MeV/nucleon excitation energy. The average kinetic energies of the different charged particles are also rather well reproduced over the whole excitation energy range (fig. 5) but the model fails to accurately follow the dependence on the different species especially for alphas. The dashed lines in fig. 5 indicate the average kinetic energies, $3T/2$, expected for an ideal gas, which appear as a rather good approximation; this is due to the low den-

sity of the emitting source. We are in presence of a quantum weakly-interacting gas.

3 Experimental event sorting

Multifragmentation is by essence associated to the emission of several fragments. Any study of the phenomenon requires a coincident and efficient detection of these fragments and of the associated particles ($Z \leq 2$). This is why, in the recent years, multifragmentation studies were performed with 4π detectors. These do not however guarantee a full detection in all reaction configurations. The combined geometrical efficiency (due to dead zones between detection cells and the necessary free space close to 0 and 180° to allow beam propagation) and detection/identification thresholds of charged particle (CP) arrays for instance, strongly disfavour any correct detection of the most peripheral collisions for energies above ~ 20 MeV/nucleon; indeed the projectile residues, emitted very close to 0° , escape detection, while the low energy of the target residues makes them unidentifiable, except if their time of flight is measured. Moreover for heavy systems a very large number of neutrons is emitted before the release of any light charged particle as shown in fig. 6. Coupling a 4π CP array to a neutron ball partly remedies this last drawback.

For an efficient study of multifragmentation, the notion of complete event was proposed: a high enough part of the reaction products should be correctly detected and identified. For central collisions, a condition on the total detected charge (more than 70-90% of the system charge) is set. For quasi-projectile, one requires the detection, in the forward centre of mass hemisphere, of a large fraction of the projectile charge, or momentum. Owing to the non-detection of neutrons, a pseudo momentum, ZV , is sometimes used, replacing the mass of each product by its charge. In any case, the representative character of the selected events should be verified.

Studies on multifragmentation should apply to homogeneous samples of events, which requires an appropriate sorting; this is mandatory for thermodynamical studies for instance. In hadron-nucleus collisions all events have similar topological properties independently of the impact parameter, as a single hot nucleus is created after a more or less abundant preequilibrium emission. Conversely, in heavy-ion collisions, the outgoing channel is different depending on the masses and asymmetry of the incident partners, the incident energy and the impact parameter. At intermediate energies residual interactions (NN collisions) strongly compete with mean field effects; the number of NN collisions largely fluctuates, leading to different final reaction channels for the same initial conditions. The weakening of the mean field hinders, on average, full stopping above about 30 MeV/nucleon; the large fluctuations mentioned above allow however the observation of "fusion" (one outgoing heavy fragment) at

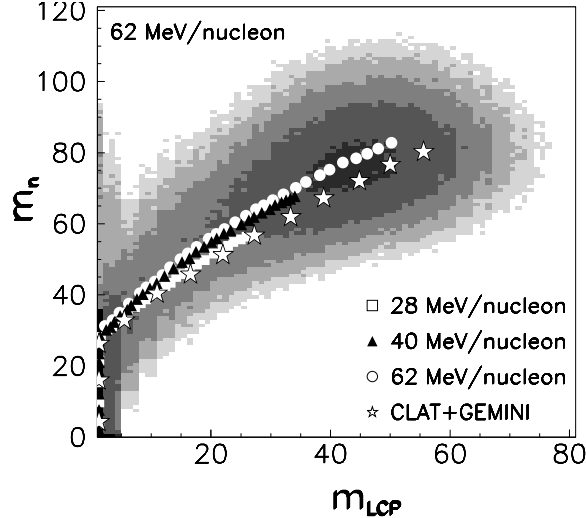


Fig. 6. Neutron vs light charged particle multiplicities for Xe+Bi reactions at various incident energies. Larger multiplicities correspond to more violent collisions. From [39]

higher energies, although with small cross sections [38]. Most of the collisions end-up in two remnants coming from the projectile and the target - accompanied by some evaporated particles -, and some fragments and particles with velocities intermediate between those of the remnants: these are called mid-velocity products. They may have several origins, e.g. direct preequilibrium emission from the overlap region between the incident partners, or a neck of matter between them which may finally separate from QP or QT, or both. Whatever the type of reaction is, a fraction of the incident translational energy is transformed into “excitation energy”, E^* , which may be shared into thermal energy (heat) and collective energies (rotational, expansion. . .). While several experimental methods give access to E^* , the knowledge of the fraction allotted to thermal or collective energies relies on models. The sorting of events, is generally done through global variables, which condensate the information measured on each event. Two philosophies guide the methods used for event sorting: the impact parameter dependence, and the event topology.

3.1 Impact parameter selectors

Sorting events with respect to an “experimental” impact parameter, b_{exp} is appropriate for studying global properties of collisions versus their violence. These methods are also useful for comparisons with transport codes, provided their outputs are filtered and sorted accordingly. Some observables are strongly connected to the impact parameter and are thus commonly used as sorting variables. One of the most popular impact parameter selector (IPS) is the charged product multiplicity [40], sometimes reduced to the - barely

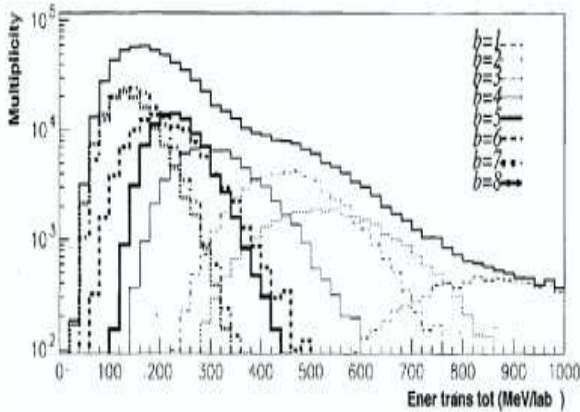


Fig. 7. Total transverse energy distributions for various impact parameters, calculated in the DYWAN simulation, for the 95 MeV/nucleon Ar+Ni system. (private communication from F. Sébille).

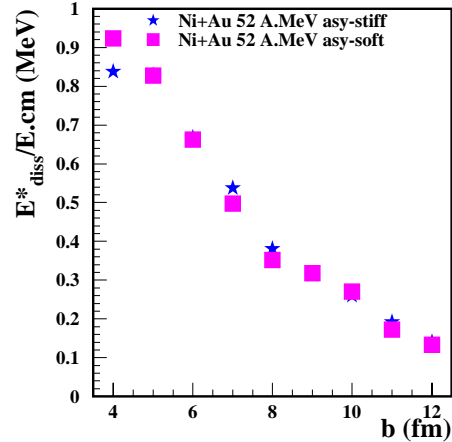


Fig. 8. Relation between the dissipated energy, E_{diss} (see text), and the impact parameter for the Ni+Au reactions at 52 MeV/nucleon modelled with a stochastic mean field simulation. From [45]

smaller - light charged particle (lcp, $Z=1,2$) multiplicity. The fragment ($Z \geq 3$) multiplicity is in no way a good selector, because its small value, less than 10, induces too large fluctuations. IPS based on coupled neutron and lcp multiplicities are used with neutron balls [41, 42]. Other IPS are the total charge bound in charged products, excluding hydrogen isotopes, $Z_{bound} = \sum(Z \geq 2)$, introduced by the ALADIN group [43], or the value of the largest charge forward emitted in the centre of mass [44], Z_{max}^{AV} . This last variable requires arrays able to identify products in a very large range of atomic number and angles. Implicit in the previous IPS is the notion of dissipation, namely the part of the initial translational energy transformed into excitation energy of the system. Several IPS reflect more directly this connection, and first of all the transverse (perpendicular to the beam) component of the energy, either of all products [46], or of lcp only [47]. The latter choice is due to the generally better efficiency of the arrays to lcp than to fragments. At intermediate energies, a narrow zone of b_{exp} generally covers a broad range of true impact parameters, as shown in fig. 7, obtained with the DYWAN code [48]. for the Ar+Ni system at 95 MeV/nucleon. If Z_{max}^{AV} is identified, its velocity, $V_{Z_{max}^{AV}}$, can be used to quantify dissipation [49]. A related variable is the energy dissipation calculated as if the reaction was purely binary, without mass transfer[50]: $E_{diss} = E_{cm} - 1/2 \mu V_{Z_{max}^{AV}} \times (A_P + A_T)/A_T$. Fig. 8 shows for instance the good correlation between the impact parameter and E_{diss} , calculated in stochastic mean field simulations for the Ni+Au reactions at 52 MeV/nucleon, despite the presence of mid-rapidity emission in the simulation; in this figure stars and squares correspond to simulations with different isospin terms in the EOS [51]. Finally correlations between the studied variables and the sorting variables

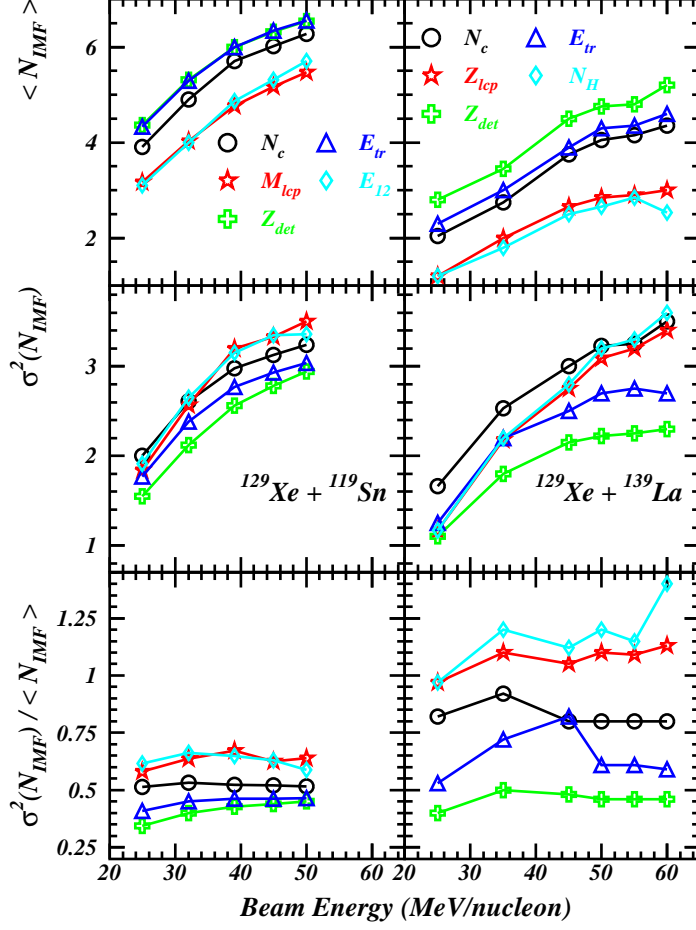


Fig. 9. Means, variances and normalized variances of the fragment ($Z \geq 3$, left) or IMF ($3 \leq Z \leq 20$, right) multiplicities versus the beam energy for central collisions between ^{129}Xe and ^{nat}Sn (INDRA data) and ^{129}Xe and ^{139}La (from [52]), using different IPS: multiplicity of charged products, N_c , of lcp, M_{lcp} , of hydrogen, N_H , total detected charge, Z_{det} , charge bound in lcp, Z_{lcp} , transverse energy total, E_{tr} , or of lcp, E_{12} .

must be avoided as much as possible. A detailed study on this subject was published in [52], where the average and the variance of the fragment multiplicity distributions obtained when selecting central collisions with different IPS (upper 10% of the IPS distribution) were examined. The authors found that M_{IMF} was positively auto-correlated (small variance and normalized variance) with the total detected charge and negatively auto-correlated (small variance and large normalized variance) with variables related to lcp or proton multiplicity. They conclude that the more neutral selectors were the charged product multiplicity and transverse energy (fig. 9). These conclusions on the best IPS are detector dependent: the same study, on a similar system but using the INDRA array, shows that the negative correlation with lcp related variables weakly persists. The total detected charge (complete events)

is, for this system, an IPS as neutral as the charged product multiplicity and total transverse energy.

3.2 Topology selectors

IPS classify events with respect to the violence of the collisions, related to the energy transformed into thermal energy, irrespective of the kind of reaction which happened. Indeed, at intermediate energies (10-100 MeV/nucleon), there are large fluctuations in the exit channel associated to a given impact parameter, as shown in stochastic transport models [53]. For this reason, and particularly when it appeared desirable to work on a rather well defined “source”, sorting variables related to the topology of the events, *namely to their shape in velocity space*, were proposed. Most of the following variables are borrowed from high energy physics.

The flow angle, θ_{flow} , is the angle between the beam axis and the main axis of the kinetic energy-flow tensor [54], $Q_{ij} = \sum_{n=1}^{M_{tot}} p_n^i p_n^j / 2m_n$, with m_n the mass and p_n^i the i^{th} Cartesian component of the momentum of particle n . The eigenvectors of the tensor define an ellipsoid, which corresponds to a rotated reference frame with respect to the centre of mass. The flow angle is connected with the impact parameter [55]. By analogy with the evolution of low energy deeply inelastic collisions, it is expected that this angle increases with the violence of the collision while the exit channel is dominantly binary; around the Fermi energy the rotation angle of the system remains small so the bulk of the cross section is associated to small flow angles. If “fusion” occurs no privileged direction is expected, so this type of events is better isolated for large flow angles. This selection was largely used in the INDRA collaboration for the study of compact single source events.

Among shape global variables are the isotropy ratio, R_{iso} , and the energy ratio [56], E_{rat} :

$$R_{iso} = \frac{2 \sum_n |\mathbf{p}_n| \sin \theta_n}{\pi \sum_n |\mathbf{p}_n| \cos \theta_n} \quad E_{rat} = \frac{\sum_n E_n \sin^2 \theta_n}{\sum_n E_n \cos^2 \theta_n} \Big|_{y \geq y_{cm}},$$

where θ_n is the emission angle of particle n in the centre of mass (or in the ellipsoid) frame, and E_n its kinetic energy. Both R_{iso} and E_{rat} quantify the part of the momentum or energy transferred from the beam to the transverse direction; they are thus equal to zero for peripheral collisions and take large values for the more central collisions, associated to more spherical shapes. Large flow angles, and R_{iso} or E_{rat} values close to 1 equally select events with compact shapes. A very powerful variable, which would deserve a larger utilisation, is the charge density, $\rho_z(k) = \sum Z_i(k) / \sum Z_i$, where k is the centre of mass velocity of particle i (with charge Z_i) [57]. With this variable it is possible to isolate rare events which are either binary - without mid-rapidity emission - or

monosource, from the majority of events which exhibit a mid-rapidity component between quasi-projectile and quasi-target remnants. All these selections implicitly assume the isotropy - or at least the forward-backward symmetry - of any source emission.

3.3 *Multivariate analysis techniques*

Event selections with both IPS and topology selectors are made *via* a sharp cut-off in the distribution of one or two variables. While it has the advantage to be simple and transparent, the physical implications might be more difficult to evaluate due to the large fluctuations of most of the global variables. A generalisation to more variables is given by the multivariate analysis techniques [58]. Principal Component Analyses allow reduction of the dimensionality of the information, and are based on a set of global variables. The multidimensional space is rearranged on axes which are linear combinations of the initial global variables, and carry a more or less important part of the information. Projecting the events on the plane defined by the two axes bearing maximum information allows to separate classes of events with a rather close topology [21, 59]. Discriminant Analyses, neuronal networks [60, 61, 62] aim at discriminating types of events. They need a learning phase before being applied to a physical problem, which is often performed with the help of a model [63, 64], but can as well directly utilize a sample of real events [65, 66]. Indeed if the model used does not correctly consider and weigh all the possible reaction channels, the final results may be biased. The advantage of these methods is that they generally provide samples of events with a higher statistics than the sharp-cut ones. The properties of the samples must however be studied in detail in order to be sure to have selected an homogeneous ensemble of events.

3.4 *Cross sections*

The knowledge of absolute cross sections is of great interest, whether one sorts events with an IPS or isolates one emission source. In the first case, for a comparison of experimental results with those of a transport code, the knowledge of the correct zone of impact parameter is mandatory. Indeed an experimental impact parameter, b_{exp} , is estimated with the help of a variable Φ assumed to vary monotonously with b , using a geometric prescription [67]:

$$b_{exp}(\Phi) = \frac{b_{max}}{\sqrt{N_{ev}}} \sqrt{\int_{\Phi_1}^{\Phi_{max}} \frac{dN}{d\Phi} d\Phi}$$

In the above formula, Φ decreases for increasing values of b , from a value Φ_{max} for $b=0$ to 0 for $b = b_{max}$. Obviously b_{exp} can be compared to the true impact parameter only if b_{max} is associated to the reaction cross section, or if the total measured absolute cross section is known. In the case of the study of a source properties, the interest is to find out whether the observed phenomenon is dominant or rare.

3.5 Conclusion

It was shown in this section that, when dealing with the results of powerful 4π arrays, it is necessary to sort the data. Several methods are used by different groups, based on global variables which condensate the information. The adequate sorting differs depending on the type of analysis which is foreseen, either an evolution with the violence of the collision and a comparison with dynamical simulations, or a thermodynamical study of the properties of a source. As an example, for central collisions, it is known that topology selectors and IPS do not select the same events, due to fluctuations in the reaction mechanism associated to a given impact parameter; while the former isolate "compact shape events", IPS favour events with elongated shapes in velocity space. It must also be stressed that *any* sorting is detector dependent, even if the "same" global variable is adopted; this must be kept in mind when comparing data obtained with different experimental set-up.

4 Fragment properties

In this section several fragment properties will be discussed, either static like multiplicities or charge distributions, or dynamical. The "references" are chosen as raw as possible, namely the total system or the projectile masses, and the available centre of mass energy, to facilitate comparisons with dynamical simulations. The main trends displayed in this section are however representative of those found for the properties of well isolated emitting sources versus the excitation energy, as it will appear in the next sections.

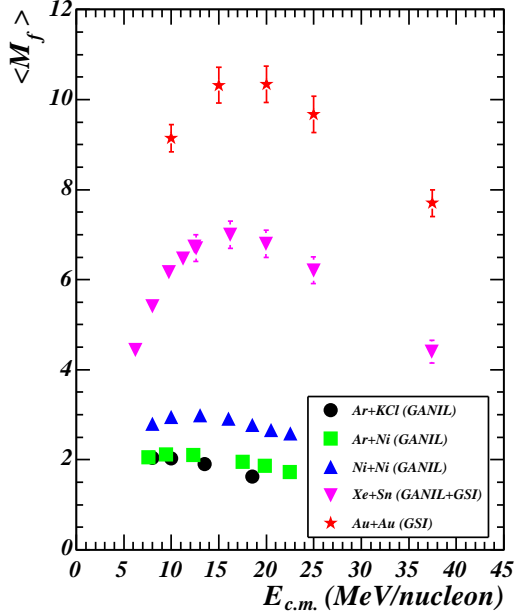


Fig. 10. Average fragment ($Z \geq 3$) multiplicities as a function of the centre of mass energy for central collisions and systems of various sizes, measured with INDRA. Statistical error bars are smaller than the size of the symbols. Systematic errors are reported for the GSI data.

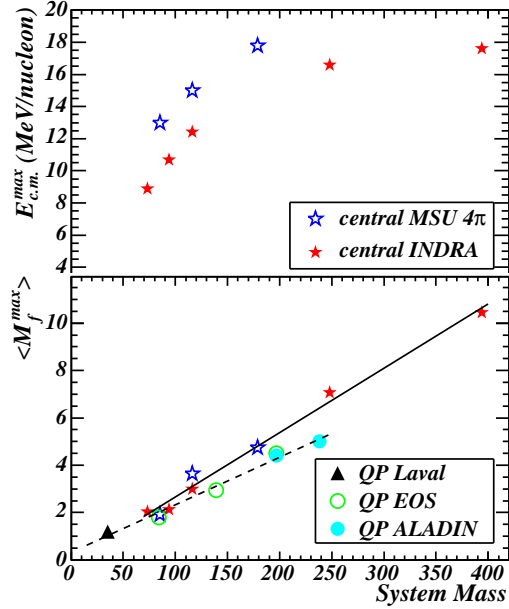


Fig. 11. Maximum average fragment multiplicities (bottom panel) and the centre of mass energy of its occurrence (top panel) for systems of various sizes. Central collisions (stars) measured with INDRA and the MSU 4π array; quasi-projectiles (circles) measured by EOS, ALADIN and Laval [18]. The lines are linear fits of central (full) and QP (dashed) data.

4.1 Multiplicities

The fragment multiplicities in multifragmentation were abundantly studied in the last years. The most prominent observation is a rise and fall of the average fragment multiplicity, observed since the early 90's for Au quasi-projectiles [68] and for Au+Au central collisions [31]: below 100 MeV/nucleon the fragment multiplicity increases when going from peripheral to central collisions, while above that beam energy the maximum fragment multiplicity is observed in semi-central collisions. The absolute maximum value is however reached in central collisions at rather moderate energy. A first study of the evolution of the IMF ($3 \leq Z \leq 20$) multiplicity versus the bombarding energy and the size of the system was performed for central collisions in [69]. In the same line, we show in fig. 10 similar results obtained with the INDRA array operating at GANIL and GSI. Central collisions were selected, as in [69], by a cut of the top 10% of the total transverse energy distribution; we chose here to present fragment multiplicities, M_f , fragments being defined as all fully identified products with a charge $Z \geq 3$. The identification thresholds are re-

spectively 0.8, 1.1, 1.3, 1.7 MeV/nucleon for $Z=3, 10, 20, 50$. Lowering all thresholds below 0.8 MeV/nucleon for all species would increase the average multiplicities by less than 3% for symmetric systems and up to a maximum of 10% for Ar+Ni at 32 MeV/nucleon. Larger multiplicities are found when the mass of the system increases. Systematic errors, essentially due to efficiency, can be estimated by requiring additionally a high completeness of the events; they lie between 0.5 and 1.5 units, increasing with the incident energy, and are larger for the GSI data due to the dysfunction of some INDRA modules. With increasing bombarding energy, the rise and fall of the average fragment multiplicity is visible in all cases (but perhaps for the lighter system Ar+KCl, where there is no rising part in the measured energy range); M_f rises rapidly at low energies up to its maximum value, M_f^{max} , but decreases smoothly on the high energy side; indeed sizeable fragment multiplicities persist in central collisions at much higher energies [70, 71]. The c.m. energy at which the fragment multiplicity is the largest also increases with the size of the system. In order to quantify these effects, the data of fig. 10 were fitted with a third degree polynomial; for comparison, the data of [69] were fitted in the same way. Figure 11 shows, as a function of the total mass of the systems, the maximum fragment multiplicity, M_f^{max} , and the energy at which this maximum occurs. The maximum multiplicities measured with the MSU 4π array and with INDRA exhibit a remarkably coherent behaviour, despite the differences in the detection devices: M_f^{max} has a value around 2 for masses 90-100, and grows further on proportionally to the total mass of the system (2.7 units of multiplicity for 100 incident nucleons). The consistency of the results indicates that M_f^{max} is little sensitive to the highest charge limit included in M_f - indeed this limit only affects the tail of the largest fragment distribution at low energies; conversely it strongly depends on the low charge threshold chosen, as shown in [72]. No saturation of M_f^{max} at the highest masses, as quoted in [69], due to the Kr+Au data of [73], is visible. The energy where M_f^{max} is observed first rapidly increases with the system mass, then tends to level off beyond mass 150 for the INDRA data. Note that $E_{c.m.}^{max}$ is systematically higher for the MSU data, although its evolution with A_{sys} is parallel to that of the INDRA data. $E_{c.m.}^{max}$ is also sensitive to the low charge limit included in M_f , decreasing when this limit is raised. The increase of the degree of fragmentation with the available energy is expected if thermal or radial flow energy put in the system increases. When it becomes very high, more hydrogen and helium isotopes are formed at break-up, and during the deexcitation stage, leading to a fall of the fragment multiplicity. Fragments being smaller for lighter systems can be a first reason of the early drop of fragment multiplicity for such systems.

Finally it is also instructive to compare the fragmentation of quasi-projectiles, as those studied by the Laval group, the ALADIN and EOS collaborations, with that of medium mass to heavy systems formed in central collisions, to get a first hint on the similarities or differences between the fragmentation mechanisms. The maximum QP fragment multiplicity (circles in fig. 11) rises linearly with the projectile mass; the values remain however smaller than those

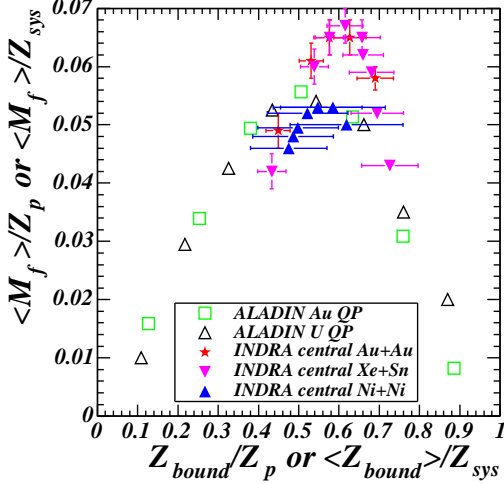


Fig. 12. Normalized average fragment multiplicities versus normalized Z_{bound} ($Z \geq 2$) for central collisions measured with INDRA and for Au and U quasi-projectiles detected with ALADIN (adapted from figs. 6 and 10 of ref. [19]). The horizontal error bars for the INDRA data represent the RMS of the Z_{bound} distributions.

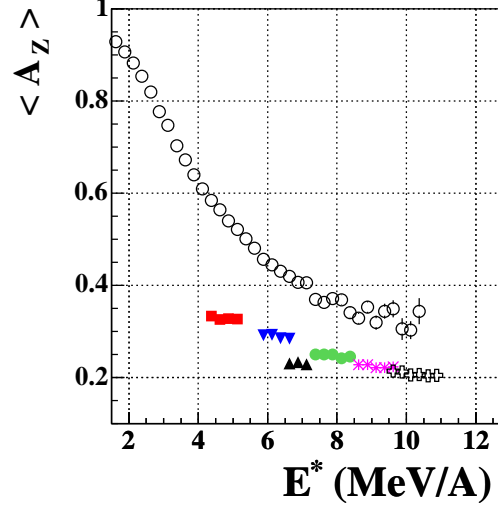


Fig. 13. Charge asymmetry of fragments as a function of the excitation energy of the emitting source, for Au quasi-projectiles (open circles), monosources from central Gd+U collisions (triangles) and Xe+Sn from 25 to 50 MeV/nucleon (other symbols). From [74]

reached in central collisions. The values of M_f^{max} for quasi-projectiles are independent of both the target mass and the incident energy [19]; this is an indication that multifragmentation is mainly driven by the thermal energy deposited in the system, as noted in [75]. The difference between the maximum multiplicities for QP's and central collisions might then come from the larger expansion energy found in the latter (see next subsection). Figure 9 of ref. [19] showed a scaling of the average fragment multiplicity versus Z_{bound} when both quantities were normalized to the projectile charge (Xe, Au or U). This scaled result is summarized in fig. 12; Z_{bound} was in that case taken as an IPS. For central collision samples measured with INDRA and used in this section, the average multiplicity and Z_{bound} (and its RMS) were normalized to the total charge of the system: a scaling is also observed for the Xe+Sn and Au+Au systems, but fails for Ni+Ni ($Z_{tot}=56$), whereas it persists for Xe quasi-projectile ($Z_p=54$) [19]. The fragment multiplicity- Z_{bound} scaling is thus a property of multifragmentation and not just a geometrical property when Z_{bound} is taken as an IPS. As already observed, for heavy systems, the scaled maximum multiplicity is higher in central collisions and occurs at higher scaled Z_{bound} , meaning that the multifragmentation partitions are different in both types of collisions. This is confirmed in fig. 13, where the average charge asymmetry of fragments, $A_Z = \sigma_Z / (\langle Z \rangle \times \sqrt{M_f - 1})$ is plotted versus the excitation energy of QP sources or monosources [74] (see sect. 6 for the calculation of E^*): the asymmetry is smaller for monosources formed in central collisions,

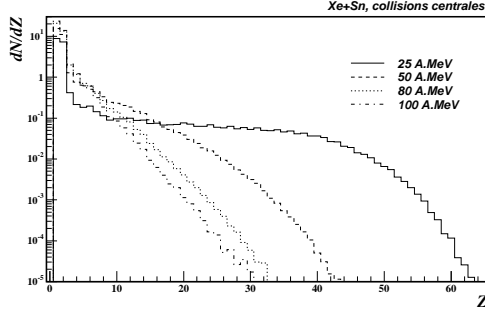


Fig. 14. Charge distributions measured for central Xe on Sn collisions between 25 and 100 MeV/nucleon incident energies. From [77]

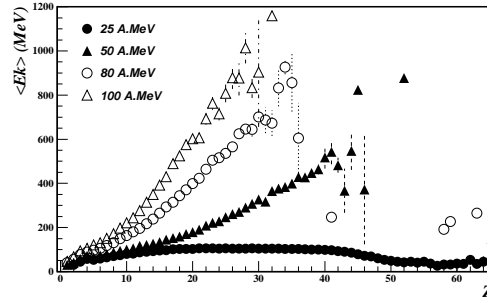


Fig. 15. Average centre of mass kinetic energy of fragments as a function of their charge for central Xe on Sn collisions (selected with the lcp transverse energy) between 25 and 100 MeV/nucleon incident energies. From [77]

which means that the system is more fragmented.

4.2 Z_{bound}^f and charge distributions in central collisions

While the fragment multiplicity exhibits a rise and fall with the incident energy, the total charged product multiplicity keeps increasing, indicating that the formed fragments become smaller. Indeed the total charge bound in fragments, $Z_{bound}^f = \sum(Z \geq 3)$, monotonously diminishes with increasing energy [72]; for heavy systems (Xe+Sn, Au+Au) the Z_{bound}^f distributions shift to smaller values and become narrower when raising the incident energy from 30 to 150 MeV/nucleon. For the Ni+Ni system it appears that the high Z tail of these distributions barely evolves above 80 MeV/nucleon. The distributions are no longer symmetric, but raise for low Z_{bound}^f , indicating that the system goes toward vaporization. The charge distributions show the same evolution, extending over a narrower charge range at higher energies, as shown in fig. 14 for the Xe+Sn system. The shape of the distribution comprises a broad plateau at moderate energies, and evolves towards an exponential decrease above 100 MeV/nucleon (see also [72]). The yield of fragments with charges $Z=3-10$ is almost independent of the incident energy, between 39 and 150 MeV/nucleon, for this system. An interesting property of the charge distributions is their independence, when scaled by the fragment multiplicity, with respect to the total charge of the (heavy) system (104 and 156 in [76]), provided that the available energy is similar.

4.3 Energy distributions - expansion

Energy spectra in the c.m. frame of fragments emitted by compact multifragmenting sources were shown in [78] for the two heavy systems 32 MeV/nucleon Xe+Sn and 36 MeV/nucleon Gd+U. They have asymmetric shapes for the lighter fragments, and tend to become more symmetric for $Z \geq 15$. These spectra bear information about the Coulomb repulsion, the radial expansion and the temperature of the source from which they originate. Indeed in [79] the Coulomb barrier deduced from the maximum of some fragment energy spectra was used to infer the density of the emitting source; a warning was made on this method by [80], where it was shown that the same shift of the maximum of the spectrum may also be due to the total Coulomb energy which increases faster than the fragment multiplicity. In any case fragment energy spectra are precious probes to test dynamical multifragmentation models [78, 81]. For compact source selection, fragment emission is roughly isotropic in the centre of mass. This is not the case for selections based on transverse energy, ACP [82] or neural networks [83]. In this case either the sources are shown to be elongated along the beam axis in coordinate space, and the fragment energy is larger in this direction, or the selection includes collisions with a binary character in the exit channel (see section 3).

The average kinetic energy of fragments as a function of their charge is thus dependent on the event selection and in some cases on the emission angle, except that of the lighter fragments which is more stable against experimental selections. For compact sources formed in central collisions between 25 and 50 MeV/nucleon Xe and Sn, the average c.m. kinetic energy is rising with the fragment charge, then saturates and even decreases for charges $Z \geq 20-25$. The decrease is essentially due to the properties of the largest fragments of the partitions. This evolution, also observed in [81], pleads for the kinetic energy essentially originating from Coulomb (and possibly radial expansion) effects rather than from thermal motion; in this latter case indeed, the average energy would be constant whatever the fragment charge or mass. Conversely with a transverse energy selection, the kinetic energy continuously increases with Z at 50 MeV/nucleon. More information was derived in [78] from the average kinetic of fragments as a function of their charge, for events sorted according to the fragment multiplicity and the rank of the fragment in the event. For each of the two above-mentioned systems, the experimental pattern was found independent of the fragment multiplicity, indicating that all emitting sources have similar charges. The largest fragment displays a specific behaviour which will be discussed later. The kinetic energy, for a given charge, increases with the collision energy, (see fig.15 and fig.39 in [81]). If the mass and the volume of the source (i.e. Coulomb effects) remain constant, then the extra energy has to come from an expansion which increases with the incident energy.

For a long time dynamical models have predicted, for central collisions between heavy nuclei, the occurrence of a compression phase followed by an

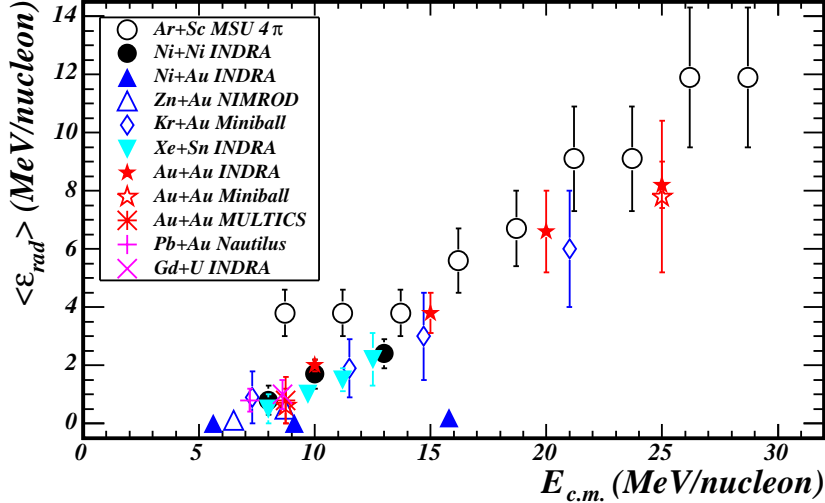


Fig. 16. Systematics of radial expansion energy per nucleon as a function of the available energy for central collisions (see text). Data are taken from: Ar+Sc [84], Zn+Au [81], Kr+Au, Au+Au MSU [85], Au+Au MULTICS [86], Pb+Au Nautilus [87] and INDRA (see text).

expansion of the system [88, 89]; the total collective energy (thermal plus compressional effects) can be derived at different times during the collision and at different distances from the centre of the expanding system. This last point gives some information about the evolution of radial velocity flow as a function of the radial distance \mathbf{r} . As for the "Big Bang" a self similar expansion (collective velocity proportional to \mathbf{r}) is observed up to (~ 80 - 100 fm/ c after the beginning of the collisions, when the system is still homogeneous (pre-fragments begin to appear at that time). With such a prescription the radial expansion velocity is extracted from experiments using: $\mathbf{v}_{rad}(\mathbf{r}) = (\mathbf{r}/R) v_0$, where R is the rms of pre-fragment distances to centre and v_0 the flow velocity. The radial expansion energy $E(R)$ is related to the average expansion energy through: $\langle E_{rad} \rangle = 3E(R)/5$; v_0 and $E(R)$ are used as reference values for comparisons. Note that a Coulomb repulsion when fragments are emitted from a spherical volume of uniform density also gives a collective velocity field proportional to \mathbf{r} . Consequently the two effects can not be distinguished and radial expansions are extracted from experiments with the help of models as SMM or event generators as SIMON, assuming given volumes at freeze-out [90, 91]. When dealing with deformed sources, a different flow profile was found, $\mathbf{v}_{rad}(\mathbf{r}) = (\mathbf{r}/R)^\alpha v_0$, with α varying between 1 and 2 [92]. Expansion energy is not a generic feature of statistical multifragmentation models, the implicit assumption is that partitions result only from the thermal part of the energy and are not influenced by the flow component. This hypothesis was shown to be correct in the framework of the lattice gas model [93, 94] even when the flow energy amounts to 50% of the available energy.

A systematics of radial expansion energies derived for central collisions and

various systems in the Fermi energy domain is reported in figure 16. In most cases, it was derived from comparison with a statistical model. In [81] it was obtained by subtracting the kinetic energies obtained at low incident energy, as representative of the Coulomb component, from those measured at higher energy; for compact sources, the statistical model implies a spherical volume, while for other selections the authors used SMM with a deformed envelope, or consider only the energy at 90° in the c.m. For the INDRA data quoted in fig. 16 several determinations were made for the same systems. Average values are reported in the figure [20, 65, 82, 91, 92, 95]. Despite the differences in the methods of determination of the radial energy, a general trend emerges, namely the onset of expansion energy around ~ 5 MeV/nucleon followed by an increase with the c.m. available energy. Values remain small (≤ 1 MeV/nucleon) up to available energies around 8-9 MeV/nucleon. No clear size effect can be inferred from the available data, because of large error bars, and the difficulty to disentangle Coulomb and expansion energies. There may be an indication that there is less expansion when the entrance channel is very asymmetric, supported by the Ni+Au and Zn+Au data, but not by those on Kr+Au. Note also that radial expansion energies deduced from the BOB dynamical simulations for the Xe+Sn system at 32 MeV/nucleon and for the Gd+U system at 36 MeV/nucleon, both studied with INDRA, are in good agreement with this systematics [91].

It is much more hazardous to derive fragment kinetic energies, and expansion energies, from quasi-projectiles, as in this case the reference frame is built from the fragment kinetic properties. The indications found in the literature are however that there is no expansion for QPs as long as their *excitation* energy, ε^* , does not reach ~ 5 MeV/nucleon; for light Ar QPs, the expansion energy is reported to increase from 0.2 to 0.7-1.1 MeV/nucleon for ε^* varying between 6 and 8 MeV/nucleon [96], while for heavy Au-like nuclei an expansion of 0.8 MeV/nucleon was found at $\varepsilon^* = 6$ MeV/nucleon [97]. A similar small variation versus the excitation energy of the source was observed in hadron induced reactions on Au nuclei, with an expansion increasing from 0.2 to 0.6 MeV/nucleon when ε^* varies between 5.5 and 8 MeV/nucleon [98]. In these two cases, the extra energy can be attributed to thermal pressure only, while for central collisions between heavy ions a compression phase occurs. The drawback on the reference frame for QP's can be overcome by using relative velocities between fragments, in order to compare values from the different kinds of multifragmenting sources [74].

4.4 *The specific role of the largest fragment*

Several studies point out the specific properties of the largest fragment in each partition, be they static or dynamic. In the MMMC statistical model it was

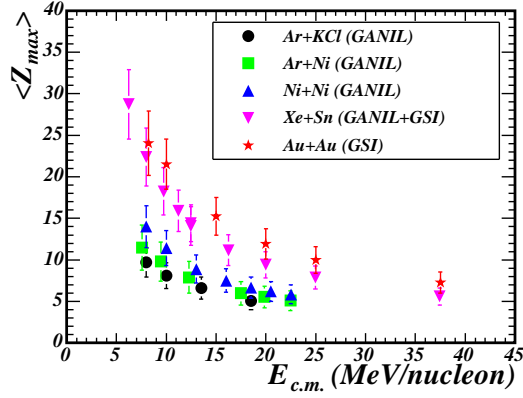


Fig. 17. Average charge of the largest fragment versus the available energy for transverse energy selected central collisions measured with INDRA.

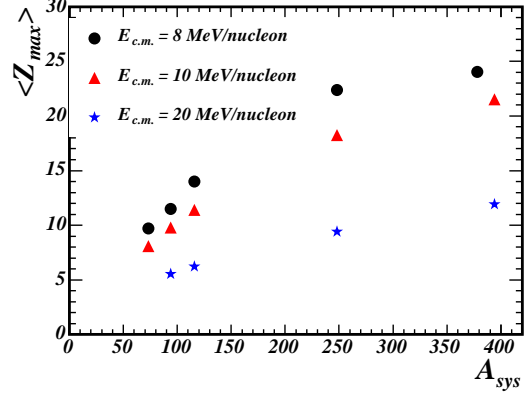


Fig. 18. Average charge of the largest fragment versus the total system mass for three available energies and central collisions.

shown that the size of the largest fragment strongly decreases with increasing thermal excitation energy of the source but is independent of the source total charge (when varied between 56 and 90); it may thus be used to estimate this energy [99]. The largest fragment size also decreases when the volume occupied by the source grows larger, as indicated in [100], while those of the fragments of higher rank are roughly constant. It must be noted that such a variation of the ranked fragments was observed when plotting the fragment size as a function of the fragment multiplicity [78].

From an experimental point of view, the independence of the largest fragment charge with respect to the system size follows from that of the charge distribution [76] and was indeed observed for the 32 MeV/nucleon Xe+Sn and 36 MeV/nucleon Gd+U compact single sources isolated among central collisions. Such a study can be extended to the central collisions studied with INDRA already used in the previous subsections (transverse energy selection). The average charge of the largest fragment, for a given system, first strongly decreases with increasing available energy and then tends to level off, due to the fixed lowest charge value $Z=3$ (fig. 17). Following models, this indicates that, as expected, the thermal energy increases with the available energy. For better evidencing the evolution with the system mass, several cuts at given available energies are performed in fig. 18; one observes that the largest fragment charge linearly rises with the system mass up to mass 180-190 above which a much smoother variation is observed (1-2 units for 100 masses). Therefore the independence of the Z_{max} distributions on the system only holds for heavy enough systems, and starting at higher mass (or charge) than in the MMC calculation.

Z_{max} also presents some specific dynamical properties. As shown in [78, 101] for selected compact multifragmenting sources, its average kinetic energy is smaller than that of other fragments with the same charge. The effect was observed whatever the fragment multiplicity for Xe+Sn between 32 and 50 MeV/nucleon

and for Gd+U at 36 MeV/nucleon. The fragment-fragment correlation functions are also different when one of the two fragments is Z_{max} (see section 7). This observation was connected to the event topology in multifragmentation, the heavier fragments being systematically closer to the centre of mass than the others. The BOB stochastic mean field simulations, which reproduce a large number of the static and dynamical properties of multifragmentation, confirm this interpretation, as shown later in fig. 29. It will be shown in the next sections that Z_{max} also displays scaling properties or bimodal distributions, indicating that it may be considered as the order parameter of a phase transition in nuclei.

4.5 *Summary on size effects*

What has been observed about the influence of the size of the fragmenting system on static variables? Firstly the maximum fragment ($Z \geq 3$) multiplicity is proportional to the system mass, for central collisions as well as for QP's. In central collisions, this maximum occurs at an energy increasing with A_{sys} up to $A_{sys} \sim 100-150$; the scaling of M_f with Z_{bound} is verified only for very heavy systems, and not for a light system with $Z_{sys}=56$; in that case it can be stressed that a very large fraction of Z_{bound} is exhausted by He nuclei (more than 40% in the explored range). The charge of the largest fragment, for a given available energy, increases with A_{sys} up to $A_{sys} \sim 190$. Thus there is not a single system mass which would be a milestone for all the variables. Finally, because of its special properties, the largest fragment must be distinguished from the others in the partition; being sure of the charge completeness of the detected events is mandatory in that aim.

5 **Theoretical descriptions of nuclear fragmentation and comparison to data**

Among the existing models some are related to statistical descriptions based on multi-body phase space calculations [37, 102, 103, 104, 105, 106, 107, 108, 109, 110, 111, 112] whereas others describe the dynamic evolution of systems resulting from collisions between nuclei via molecular dynamics [113, 114, 115, 116, 117, 118, 119, 120, 121] or stochastic mean field approaches [122, 123, 124, 125, 126, 127, 128, 129, 130, 131, 132, 133]. The first approach uses the techniques of equilibrium statistical mechanics (counting of microstates) with a freeze-out scenario and has to do with a thermodynamical description of the phase transition for finite nuclear systems. The second, in principle more ambitious, completely describes the time evolution of the collisions and thus helps in learning about nuclear matter (stiffness of the effective interaction

and in-medium NN cross-sections), its phase diagram, finite size effects and the dynamics of the phase transition. Therefore it is highly instructive to compare results of the two types of models to experimental data.

5.1 *Statistical ensembles and models*

Three different ensembles are used in statistical models; rigorously only the microcanonical ensemble is adapted to describe isolated excited finite nuclei. The grandcanonical or macrocanonical ensemble corresponds to the rougher description where the system can exchange particles as well as energy with a reservoir. In this ensemble the temperature and the chemical potential are fixed variables. The total energy but also the total number of nucleons and the total charge fluctuate from channel to channel. Constraints are only on the average mass and charge of the system. This ensemble is generally used for infinite systems and in relativistic quantum systems where particles are created and destroyed. However it is a good approximation for hot nuclei when one is not interested in an event-by-event analysis and only wants to calculate mean values at very high excitation energies ($\geq 6-7$ MeV/nucleon) where the number of particles associated to deexcitation is large [37, 107, 108, 109, 110] (see subsection 2.2). A second ensemble, the canonical ensemble, is used to describe a system with a fixed number of particles in contact with a heat reservoir at fixed temperature [106, 134, 135]. Here the total energy fluctuates from partition to partition and only the mean value of the total energy is fixed. Considering hot nuclear systems and using the Fermi gas model, one can estimate the standard deviation of the excitation energy distribution, σ , as a function of the temperature T and of the number of nucleons A . It is given by the relation $\sigma = 4E^*/\sqrt{AT}$ which shows that the canonical ensemble becomes a reasonable approximation for $A \gtrsim 200$ and temperature $T \gtrsim 6$ MeV. Within the formalisms of both these ensembles many studies have been performed to derive mean properties and to discuss phase transitions in terms of intensive variables such as temperature. The third ensemble, the microcanonical one, is the most relevant for studying isolated systems like nuclei. It is used to describe a system which has fixed total energy and particle number [104, 105, 110, 111]. In this ensemble the temperature is no longer a natural concept and a microcanonical temperature can be introduced through the thermodynamic relation: $T_{micro}^{-1} = \partial S / \partial E$. Such an ensemble is fully appropriate if one wants to study, for example, partial energy fluctuations (see section 9) and/or to perform analyses on an event-by-event basis. Results have to be discussed as a mixing of microcanonical ensembles in order to be compared to those of canonical ensembles. Numerical realizations are possible after elaborating specific algorithms based on the Monte Carlo method. Finally one can conclude about the choice of the different ensembles by saying that the excitation energy domain, the size of the system, the pertinent observable to study and the

event sorting chosen impose (or permit with some approximation the statistical ensemble to be used. For comparison with data additional constraints (volume, pressure, average volume. . .) are added to these ensembles [136, 137].

5.2 Statistical descriptions of multifragmentation

A statistical theory of multifragmentation is supposed to predict partition probabilities at statistical equilibrium. Thus the weight of a given break-up channel f , i.e. the number of microstates leading to this partition, is determined by its entropy, $\Delta\Gamma_f = \exp S_f$, within the microcanonical framework. Statistical model event generators have been developed for comparisons with experiments and in such models the set of fragments corresponding to a given partition is considered to be distributed randomly in a freeze-out volume equal to 3-10 times the corresponding volume at normal density; the freeze-out stage is assumed to follow a compression-expansion or/and a thermal expansion [138] phase. These fragments interact via Coulomb forces and are endowed with some internal excitation energies and initial thermal velocities. Radial expansion velocities, fully decoupled from thermal properties, are also added in some models. The subsequent evolution including sequential decays of primary fragments is performed, preserving in some models space-time correlations. Finally generated events are filtered to account for the experimental device. Detailed presentations of models can be found in references [17, 105, 110, 111, 112]. Within such an approach the input parameters: mass and charge of the system at break-up density, its excitation energy, its volume at freeze-out and the eventual added radial expansion have to be backtraced to experimental data, estimated from dynamical simulations or derived from data related to properties of systems at break-up. Statistical models are very useful to compare data sets and to produce comparisons or systematics. The following examples illustrate their different utilizations.

In fig. 19 the fragment charge distribution measured for central $^{129}\text{Xe} + ^{\text{nat}}\text{Cu}$ collisions at 30 MeV/nucleon incident energy [139] is compared to the Berlin Multifragmentation Model (also called MMMC-Microcanonical Metropolis Monte Carlo) [105] and to the sequential statistical model GEMINI [140]. The BMM calculations give good qualitative agreement with the experimental charge distribution over the entire Z range measured. Input parameters of the source ($A=177$, $Z=76$ and 750 MeV excitation energy) were estimated from dynamical simulations at a freeze-out time corresponding to a volume of $5.6 V_0$ ($R_{FO}=11.8$ fm for the sphere including all the products at freeze-out). Results with a larger freeze-out volume ($10.7 V_0$) which show a better overall agreement are also shown. Conversely, the GEMINI calculation underpredicts the yields of low Z by an order of magnitude and predicts a nearly flat charge distribution. A comparison with the most popular model, namely the Statistical Multifragmentation Model SMM [110], is shown in fig. 20 for the largest

fragment and the fragment multiplicity as a function of the thermal excitation energy of the source. It concerns multifragmentation of 1 GeV/nucleon Kr, La and Au projectiles produced in collisions with a carbon target, studied by the EOS collaboration [141, 142]. Inputs for SMM (thermal excitation energy, mass, charge and freeze-out volume of the source) were derived from data including p-p correlations for freeze-out volume and the ISABEL cascade model for estimate of preequilibrium neutrons, which were not detected. The ranges of mass and charge of the SMM sources which cover the explored thermal excitation energy domains are $A=80-30$ and $Z=34-16$ for Kr, $A=130-80$ and $Z=54-26$ for La and $A=190-120$ and $Z=76-48$ for Au. The standard value of SMM (16 MeV) was used for the inverse level density parameter and derived freeze-out volumes correspond to three times the volume of Kr, La and Au nuclei at normal density. In SMM the definition of the freeze-out volume differs from that of BMM and includes only the centre of all the fragments. Very good agreements are observed between data and SMM for the largest fragment over the whole range of thermal excitation energy whereas fragment multiplicities are overestimated by about 20% in the excitation energy range 5-10 MeV/nucleon. Finally fig. 21 shows different static and dynamic fragment observable distributions measured for central Xe+Sn collisions at 32 MeV/nucleon incident energy and compared again with SMM. To get this agreement the input parameters of the source are the following: $A=202$, $Z=85$ as compared to $A=248$ and $Z=104$ for the total system, freeze-out volume $3V_0$, partitions fixed at thermal excitation energy = 5 MeV/nucleon and added radial expansion energy of 0.6 MeV/nucleon. As we have shown with those examples, but it is a general trend, the observed properties of fragments are compatible with the hypothesis of sources in thermal equilibrium which undergo multifragmentation.

5.3 Dynamical descriptions of multifragmentation

Beside statistical descriptions, there are microscopic frameworks that directly treat the dynamics of colliding systems such as the family of semi-classical simulations based on the nuclear Boltzmann equation (the Vlasov-Uehling-Uhlenbeck (VUU), Landau-Vlasov (LV), Boltzmann-Uehling-Uhlenbeck (BUU) or Boltzmann-Nordheim-Vlasov (BNV) codes [144, 145, 146, 147]), classical molecular dynamics (CMD) [121, 148, 149, 150], quantum molecular dynamics (QMD) [113, 114, 115], fermionic molecular dynamics (FMD) [117], antisymmetrized molecular dynamics (AMD) [116, 118, 119] and stochastic mean field approaches related to simulations of the Boltzmann-Langevin equation [122, 123, 124, 126, 127, 128]. Boltzmann type simulations follow the time evolution of the one body density. Neglecting higher than binary correlations, they ignore fluctuations about the main trajectory of the system (deterministic description), which becomes a severe drawback if one wants to describe processes

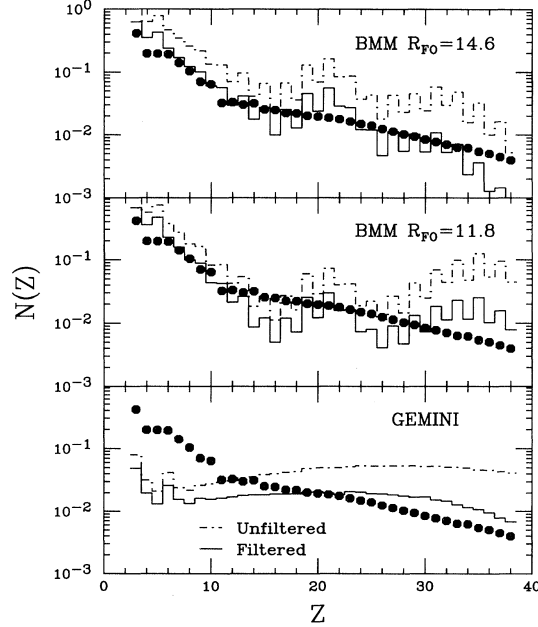


Fig. 19. Experimental charge distribution (full points) in central events compared with unfiltered (dot-dashed curves) and filtered (solid curves) predictions by the BMM model with two freeze-out radii (top and central panels, see text) and by GEMINI (from [139]).

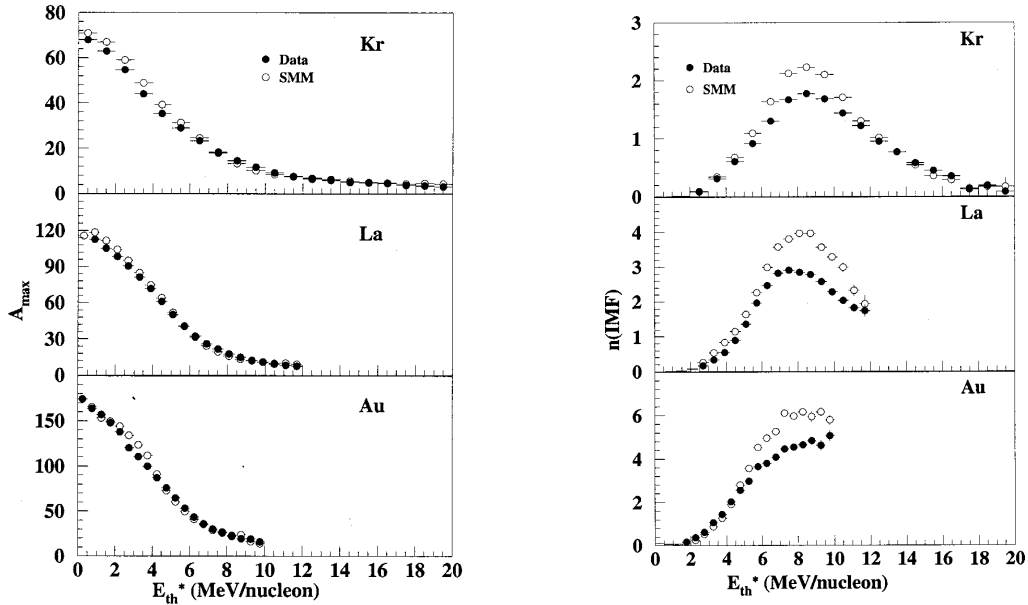


Fig. 20. Left panel: size of the largest fragment as a function of thermal excitation energy, E_{th}^* for multifragmentation of 1 GeV/nucleon Kr, La and Au (data) and SMM. Right panel: idem for average fragment multiplicities (from [142]).

involving instabilities, bifurcations or chaos expected to occur during the multifragmentation process. Such approaches are only appropriate during the first

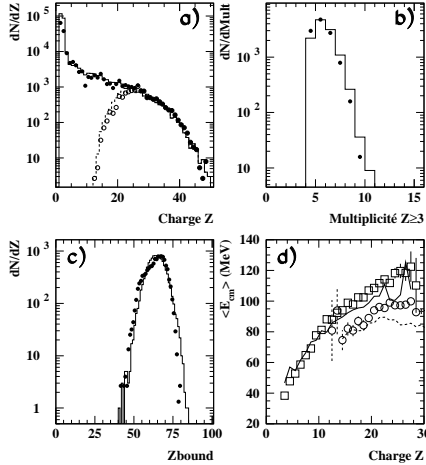


Fig. 21. Comparison of experimental data (Xe+Sn compact single sources produced in central collisions-32 MeV/nucleon) with SMM simulations. The lines are for data and symbols for SMM (all fragments, except open circles and dashed lines which refer to the largest fragment of each partition). Z_{bound} represents the sum of the charges of all fragments (from [20]).

stages of nuclear collisions, when the system is hot and possibly compressed and then expands to reach a uniform low density. They become inadequate to correctly treat the fragment formation, and for the description of multi-fragmentation it is essential to include fluctuations. This is done in quantum molecular dynamics methods and in stochastic mean field approaches.

5.3.1 Quantum molecular dynamics: QMD and AMD simulations

QMD is essentially a quantal extension of the molecular dynamics approach widely used in chemistry and astrophysics. Starting from the n-body Schrödinger equation, the time evolution equation for the Wigner transform of the n-body density matrix is derived. Several approximations are made. QMD employs a product state of single-particle states where only the mean positions and momenta are time-dependent. The width is fixed and is the same for all wave packets. The resulting equations of motion are classical. Also the interpretation of mean position and momenta is purely classical and the particles are considered distinguishable; this simplifies the collision term which acts as a random force. All QMD versions use a collision term with Pauli blocking in addition to the classical dynamics. Some versions consider spin and isospin and others do not distinguish between protons and neutrons (all nucleons carry an average

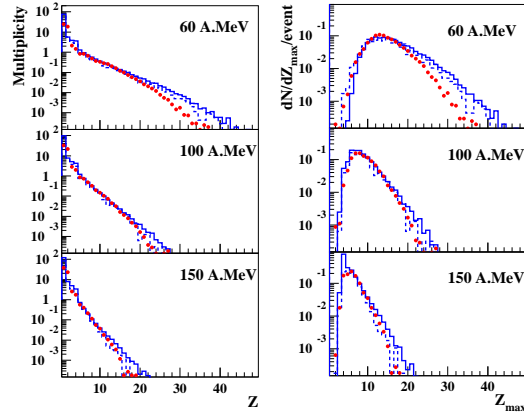


Fig. 22. Fragment (left panel) and heaviest fragment (right panel) charge distributions for central $^{197}\text{Au}+^{197}\text{Au}$ collisions at different incident energies. Points refer to data and full lines to fragment from QMD events. Fragments from QMD events filtered by the experimental device correspond to dashed lines (from [143]).

charge). Finally one has to stress that for most of the QMD versions a statistical decay code must be coupled to describe the long time dynamics. However for the code of ref. [114] there is no need to supplement the QMD calculations by an additional evaporation model [151]. This code was very recently used in a rather complete comparison with data measured for central $^{197}\text{Au}+^{197}\text{Au}$ collisions over the incident energy range 60-150 MeV/nucleon [143]. Using a soft equation of state (incompressibility $K_\infty = 200$ MeV), static properties like fragment multiplicity and charge distributions are rather well reproduced, particularly for the higher incident energies where QMD codes are certainly better adapted. Figure 22 illustrates the comparison for fragment and heaviest fragment charge distributions.

An antisymmetrized version of molecular dynamics (AMD) was constructed by incorporating two-nucleon collision process as the residual interaction into the fermionic molecular dynamics (FMD). AMD describes the system with a Slater determinant of Gaussian wave packets and therefore can describe quantum-mechanical features. However, in the dynamics of nuclear reactions, there may be other phenomena caused by the wave packet tail that are completely lost in AMD due to the restriction of the single-particle states. So an improvement was realized (called AMD-V) with the stochastic incorporation of the diffusion and the deformation of wave packets which is calculated by the Vlasov equation without any restriction on the one-body distribution [118]. More recently the quantum branching process due to the wave packet diffusion effect was treated as a random term in a Langevin-type equation of motion whose numerical treatment is much easier. Moreover a new approximation formula was also introduced in order to evaluate the Hamiltonian in the equation of motion with much less computation time than the exact calculation, so that systems like Au+Au are now treatable [152]. As for QMD the stiffness of the effective interaction and the in-medium NN cross-section are both important ingredients for determining the degree of agreement with experimental data. In order to test the sensitivity of the ingredients, a detailed study of reaction dynamics and multifragmentation was done in ref [81] by comparing AMD-V calculations with data from heavy-ion reactions around the Fermi energy. Figure 23 presents multiplicity distributions of selected particles and fragments produced in central $^{64}\text{Zn}+^{92}\text{Mo}$ collisions at 47 MeV/nucleon incident energy. Thin solid, dashed and thick solid lines indicate the results of Soft+ NN_{emp} , Stiff+ NN_{emp} and Stiff+ NN_{LM} respectively. As previously observed with QMD a better global description of data is obtained with a soft equation of state (incompressibility $K_\infty = 228$ MeV). We refer the reader to ref. [81] for more information on in-medium NN cross-section.

5.3.2 Stochastic Mean Field approach: Brownian One-body Dynamics (BOB)

In many domains of physics a diffusive behaviour is described by transport theories which were originally developed for Brownian motion. The effects of

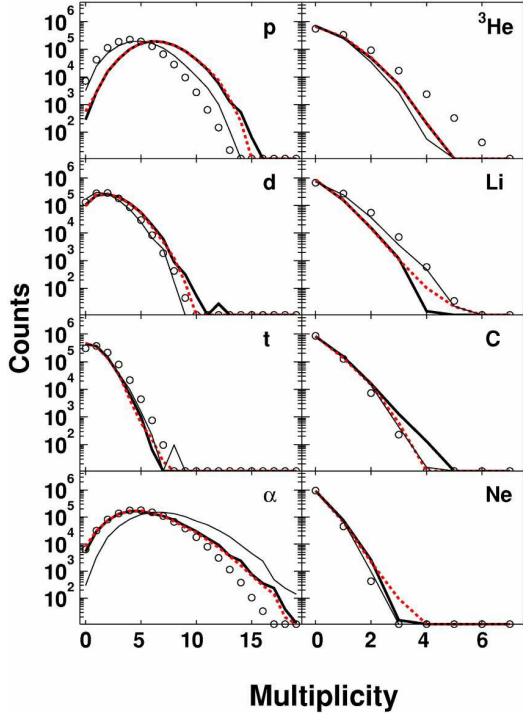


Fig. 23. Multiplicity distributions of selected particles and fragments produced in central $^{64}\text{Zn}+^{92}\text{Mo}$ collisions at 47 MeV/nucleon incident energy. Experimental results are shown by circles and calculated results (AMD-V) correspond to different lines (see text). All calculated results have been treated with the experimental filter and all distributions are normalized to one million events in total (from [81]).

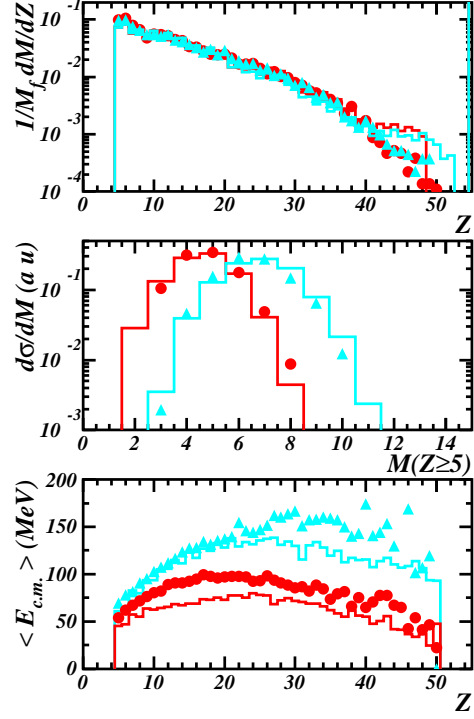


Fig. 24. Comparison of experimental data (central collisions: Gd+U-36 MeV/nucleon and Xe+Sn-32 MeV/nucleon) with BOB simulations for charge and multiplicity distributions of fragments (top and middle panels) and for their average kinetic energies (bottom panel). The symbols are for data and the lines for BOB simulations. Light grey lines and triangles stand for Gd+U and black lines and circles for Xe+Sn (adapted from [91]).

the disregarded degrees of freedom are simulated by a random term in the dynamics of the retained variables. That idea is the starting point of the so-called Boltzmann-Langevin equation (BLE): $\partial f/\partial t = \{h[f], f\} + \bar{I}[f] + \delta I[f]$ which was introduced for heavy-ion collisions in references [122, 123, 124]. f is the one-body phase space density. The first term on the r.h.s. produces the collisionless propagation of f in the self-consistent one-body field described by the effective Hamiltonian. The second term, called collision term, represents the average effect of the residual Pauli-suppressed two-body collisions; this is the term included in LV, BUU and BNV simulations. The third term is the Langevin term which accounts for the fluctuating part of the two-body collisions. Exact numerical solutions of the BLE are very difficult to obtain and have only been calculated for schematic cases in one or two dimen-

sions [125]. Therefore various approximate treatments of the BLE have been developed. The basic idea of BOB [129] is to replace the fluctuating term by $\delta\tilde{I}[f] = -\delta\mathbf{F}[f]\cdot\partial f/\partial\mathbf{p}$ where $\delta\mathbf{F}(\mathbf{r}, t)$ is the associated Brownian force ($\langle\delta\mathbf{F}\rangle=0$). Since the resulting Brownian one-body dynamics mimics the BL evolution, the stochastic force is assumed to be local in space and time. The strength of the force is adjusted to reproduce the growth of the most unstable modes for infinite nuclear matter in the spinodal region (see section 8). Quantal fluctuations connected with collisional memory effects are also taken into account as calculated in [153].

An extensive comparison data-BOB was made for two very heavy fused systems produced in Xe+Sn and Gd+U central collisions which undergo multifragmentation with about the same excitation energy (~ 7 MeV/nucleon) [72, 78, 91]. Stochastic mean-field simulations were performed for head-on collisions with a self-consistent mean field potential chosen to give a soft equation of state ($K_\infty=200$ MeV). The finite range of the nuclear interaction was taken into account using a convolution with a Gaussian function with a width of 0.9 fm. A term proportional to $\Delta\rho$ in the mean-field potential was added; it allows to well reproduce the surface energy of ground-state nuclei, which is essential in order to correctly describe the expansion dynamics of the fused system. In the collision term a constant NN cross-section value of 41 mb, without in-medium, energy, isospin or angle dependence was used. As a second step the spatial configuration of the primary fragments, with all their characteristics as given by BOB, was taken as input in a statistical code to follow the fragment deexcitation while preserving space-time correlations. Finally the events were filtered to account for the experimental device. These simulations well reproduce the observed charge and multiplicity distributions of fragments (see fig. 24). Particularly the independence of the charge distribution against the mass of the system experimentally observed was recovered [76]. More detailed comparisons of the charge distributions of the three heaviest fragments also show a good agreement [91]. Kinetic properties of fragments are rather well reproduced for the Gd+U system, whereas for Xe+Sn the calculated energies fall $\sim 20\%$ below the measured values. We also refer the reader to sections 7 and 8 for further comparisons.

5.3.3 Concluding remarks on dynamical simulations

To conclude on dynamical descriptions of multifragmentation one can make a few general comments. Better agreements between data and calculations are generally observed with a soft equation of state (incompressibility $K_\infty \sim 200-230$ MeV). One can however not trust the in-medium NN cross-sections extracted as the self-consistency between the mean field potential and the two-body collision term is not fulfilled in models. QMD and AMD calculations lead to too much transparency at low incident energies (typically below 50-100 MeV/nucleon). For AMD-V and BOB calculations at incident ener-

gies around 35 MeV/nucleon a maximum density of 1.2-1.4 ρ_0 is observed at 30-40 fm/c after the beginning of central heavy-ion collisions and the normal density is recovered around 70 fm/c. Thermal equilibrium times are found in the range 100-140 fm/c after the beginning of collisions, well before freeze-out configurations (200-300 fm/c). Primary fragments exhibit an equal or almost equal excitation energy per nucleon of 3-4 MeV. The mechanism of fragment production differs depending on model type. In molecular dynamics models fragments are preformed at early stages close to the normal nuclear density whereas in stochastic mean field calculations, as BOB, fragment formation is linked to the spinodal decomposition mechanism: mononuclear systems at low density ($\sim 0.4\rho_0$) formed at around 100 fm/c develop density fluctuations during about 100 fm/c to form fragments. More constrained observables related to the formation of fragments by spinodal instabilities will be discussed in section 8.

Last point, dynamical calculations exhibit radial collective energies for fragments with average values in the range 0.1-2.0 MeV/nucleon for heavy-ion collisions in the Fermi energy domain which fairly agree with values derived from experiments (see subsection 4.3).

5.4 *The link between dynamical and statistical descriptions*

While both descriptions show reasonable agreement with data in reproducing average static and kinematic properties of fragments, sharp conclusions on multifragmentation scenarii can not yet be derived. However from dynamical descriptions like AMD-V and BOB we learnt that, in average, thermal equilibrium was reached before the breaking stage, which is also the hypothesis of statistical approaches. A tentative to derive more precisely at what time, during the reaction, the statistical description takes place was done in refs. [78, 154]: in BOB simulations of Xe+Sn central collisions at 32 MeV/nucleon incident energy, the volume of the system was calculated every 20 fm/c from 100 to 250 fm/c to be compared with the freeze-out volume of $3V_0$ as input in the SMM code [78, 154]. The result is the following: at 200 fm/c, during the formation of fragments, a freeze-out volume of $\sim 3V_0$ (calculated à la SMM) is reached and the characteristics in size of the source are $A=190$ and $Z=80$, in good agreement, within 10%, with SMM inputs. Very recently a remarkable result was also obtained by checking the consistency of predictions between the dynamical evolution of Xe+Sn central collisions at 32 MeV/nucleon via a stochastic mean field approach and a microcanonical multifragmentation model (MMM) [155]: a statistically equilibrated stage was identified at ~ 140 fm/c just intermediate between the beginning of the spinodal decomposition and the freeze-out configuration. In both cases a rather coherent link between dynamical descriptions, like stochastic mean field approaches, and statistical descriptions is derived.

6 Calorimetry and thermometry

The knowledge of the excitation energy and temperature, as well as of its numbers of neutrons and protons (mass and charge) is mandatory for any description of a system in terms of thermodynamical variables. Determining these quantities remains the most challenging task for the groups involved in the study of multifragmentation.

As previously mentioned, in nuclear collisions the formed multifragmenting systems are accompanied by a quite abundant preequilibrium emission. These early emitted products should not be included in the calculation of the mass and of the excitation energy of the fragmenting system; it is unfortunately difficult to unambiguously attribute the observed final products to preequilibrium or to the fragmenting system. This is particularly true for neutrons - when measured - and for light charged products, H and He and to a lesser extent Li and Be isotopes. Conversely the properties of the heavier fragments indicate that they do originate from the fragmenting system. Preequilibrium is removed either with the help of models, or through angular and energetic properties of the observed products [77, 91].

6.1 Calorimetry

All procedures for obtaining the excitation energy of a fragmenting source, observed with a 4π array, are based on the determination of its velocity. For central collisions the reaction centre of mass velocity is most often chosen whereas the quasi-projectile velocities are identified to either that of the biggest fragment, or that of the subsystem containing all the fragments ($Z \geq 3$ or 5), forward emitted in the centre of mass. The excitation energy, E^* , of the source is then calculated event by event with the relation $E^* = \sum_{M_{cp}} E_{cp} + \sum_{M_n} E_n - Q$. E_{cp} and E_n are respectively the kinetic energies of charged products and neutrons belonging to the source, Q is the mass difference between the source and all final products. Energies are expressed in the source reference frame. M_{cp} is in most cases the detected multiplicity of charged products. The energy removed by gamma rays is small and most often neglected in the calculation. The decision of including or not one observed charged product in the source differs with the experimental apparatus and the type of collision under study.

CC for central heavy-ion collisions, all fragments with $Z \geq 3$ (or 5) are attributed to the source. Preequilibrium in that case is mostly forward/backward emitted, and indeed the angular distributions of the light products appear isotropic between 60 and 120° . The charge, mass and energy contributions of these particles are doubled for the calculation of the characteristics of the source (i). Another possibility, to account for the detector inefficiency, is to calcu-

late the charge, mass and energy of the anisotropic part, and to remove it from those of the composite system (ii).

QP for quasi-projectiles the most important contamination comes from mid-rapidity products and several techniques are used for the QP reconstruction.

i) All fragments forward emitted in the reaction c.m. system are attributed to the QP. Variants consist either in putting a low velocity cut for the lighter fragments [156, 157], or in keeping only events with a compact fragment configuration in velocity space [74, 158]. Then twice the light elements in the QP forward hemisphere are added. ii) Fragments are treated as above, but particles are attributed a probability to come from the QP emission, either using a 3-source fit [42], or by taking a well characterized subspace as reference [50, 159]. The velocity of the QP is then recalculated by including all its components.

hIC finally in hadron-induced collisions, products emitted from the source are chosen from energetic considerations, by excluding those with an energy per nucleon above a given threshold either fixed [160] or varying with Z [161].

All those procedures assume forward-backward symmetry of particle emission in the source frame. For QP's the symmetry of the source emission may be questionable when highly excited QP's and QT's start emitting right after their separation [162, 163]: the close proximity of the partner deforms phase space and emission is favoured between the QP and QT. This possible effect is generally ignored.

Once counted the charged products, the charge of the source is known. A first uncertainty is introduced in calculating the associated mass, as that of heavy fragments is not measured. A single mass is attributed to all nuclei with a given atomic number, either that of the most stable species, or that derived from formulae existing in the literature (EPAX [164] or EAL [165]). At that point neutrons must be included. Except in experiments using a neutron ball, neither their multiplicity nor their energy is known. The neutron number is thus calculated by assuming that the source has the same N/Z ratio as the total system (central or hadron-induced collisions) or as the projectile. The average neutron energy is taken equal to the average proton energy over the event sample, removing some Coulomb barrier. Note that with neutron balls only the neutron multiplicity is measured, at the price of a poor geometrical coverage for charged products. In that case corrections accounting for the undetected particles and neutrons are made [39].

In central heavy-ion reactions, the excitation energy domain populated is narrow : $\sigma_{E^*} \sim 0.7-1.25$ MeV/nucleon; the width includes experimental effects (detector efficiency and resolution), calculation assumptions and physical effects (pre-equilibrium). Conversely, in hadron-induced reactions as well as in quasi-projectile studies, a broad domain of excitation energy is populated, proportionally to the partial cross section, function of the impact parameter. However, due to on-line trigger effects, very low energies are poorly sampled, by particular events matching the trigger requirement; indeed neutron emis-

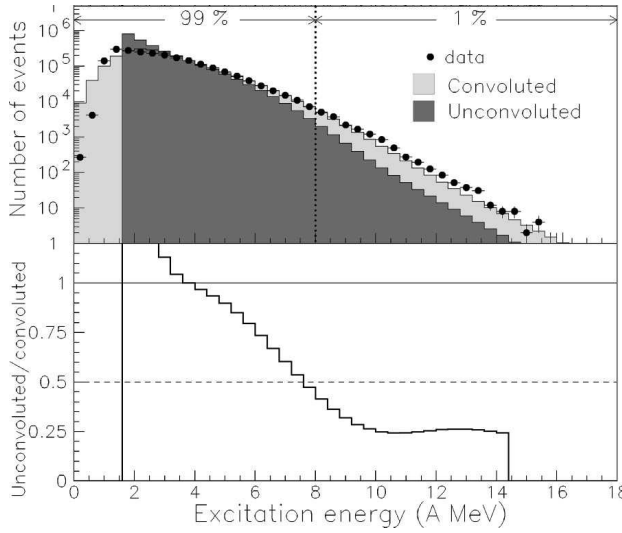


Fig. 25. Top : Convoluted, unconvoluted and experimental excitation energy distributions obtained in π +Au reactions. Bottom : Ratio of unconvoluted-to-convoluted distribution as a function of the excitation energy per nucleon. Adapted from [166]

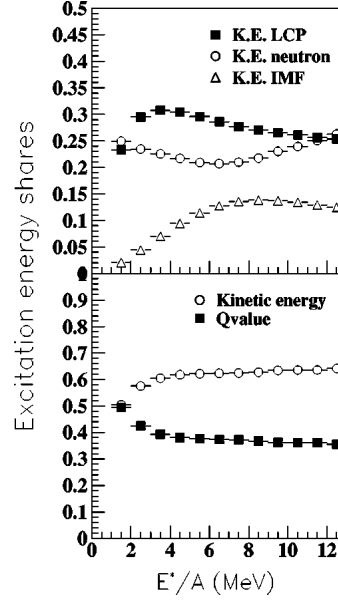


Fig. 26. Relative share of excitation energy for various components of the reconstruction procedure as a function of the excitation energy per nucleon. From [166]

sion - not detected - is dominant in this region. At the other end of the distribution, the very high energies probably result from significant fluctuations. In all cases the reliable domain extends from about 2 to 8 MeV/nucleon: for example in fig. 25 obtained in π +Au reactions, the excitation energy distribution is unconvoluted assuming Gaussian fluctuations. More than half of the 1% of events above the vertical dotted line have an energy overestimated by 1-2 MeV/nucleon [166].

How reliable are the energies so obtained ? Because of compensation of the errors on the mass and on the energy, the energy per nucleon is a more robust experimental observable than the energy. By comparing values obtained by different methods for quasi-projectiles, differences on E^*/A smaller than 10% were found [74, 167]. From simulations with the HIPSE event generator, the reconstructed values were found to differ from the true values by less than 10%, except for very peripheral collisions where the discrepancies are much larger [159]. In central collisions, excitation energies slightly smaller than the available energies are generally found, which is what can reasonably be expected. It was verified in the INDRA Xe+Sn data that procedures CCi and CCii give the same results when a high degree of completeness is required for CCi, e.g. 90% of the system charge. For lesser completeness (80%), the difference between both types of calculation increases with the incident energy, reaching 1 MeV/nucleon (10%) at 50 MeV/nucleon. The main source

of uncertainty in the calculation of E^* comes from the neutron terms. However, compensation occurs in the calorimetry equation between the kinetic and the mass balance terms; indeed the weight of these two terms is similar for quasi-projectiles and in hadron-induced reactions ($Q/E^* \sim 30\text{-}36\%$ [74, 166] - see fig. 26); in central collisions the Q term accounts only for $\sim 20\%$ of the excitation energy.

6.2 Temperature measurements

Two recent reviews extensively describe the methods used for temperature measurements [168, 169, and references therein]. A brief summary will be given here. The concept of temperature for a nucleus, which is a microscopic, isolated Fermionic charged system, is not *a priori* obvious. According to statistical mechanics, temperature can be defined as $T^{-1} = \partial S(E, N, V)/\partial E$, where S , E , V , N , are the entropy, energy, volume and (fixed) number of particles of the system. This definition is valid only if the system is in statistical equilibrium and its density of states is known. For compound nuclei at low excitation energy, both conditions are fulfilled, which might not be the case at higher energies, and for fragments resulting from multifragmentation. Moreover no probe can be used to measure the temperature of these small systems, it has to be derived from the properties of particles that they emit during their cooling phase. The abovementioned issues of identifying an equilibrated emitting source by distinguishing pre-equilibrium particles from those emitted by that source is therefore common to all the methods. Three families of methods are used to "measure" temperatures.

- (1) *Kinetic approaches.* Historically, temperatures of compound nuclei were derived from the slopes of the kinetic energy spectra of the emitted neutrons or charged particles that they evaporate, as the spectra can be fitted with Maxwell-Boltzmann distributions. At higher energies, when long chains of particles are emitted, the obtained result is an average over the deexcitation chain, and may differ from one particle to another, depending on the emission sequence. To retrieve the initial temperature, it was proposed to subtract from the spectra those of particles coming from the same nucleus formed at lower excitation energies [170]. For multifragmenting systems, the slopes of light product spectra lead to very high "temperatures", and do not probably reflect only the thermal properties of the system, but also the collective energies coming from the dynamics of the nuclear collision. It was recently proposed to derive the temperature of the fragmenting system from the slope of the thermal hard photons [171], which have the advantage of being insensitive to Coulomb field and final-state effects: temperatures close to 7 MeV are for example obtained for central Xe+Sn collisions at 50 MeV/nucleon.

- (2) *Population of excited states.* The underlying idea for this method is that the population of the excited states of a system in statistical equilibrium is given by the temperature of the system and the energy spacing, ΔE , between the levels. This definition in itself bears the limits of the method: when the temperature is higher than ΔE , the ratio between the population of two states saturates. Considering particle-unbound states is thus interesting as it allows to measure higher temperatures, and the population ratio should in that case be less influenced by secondary decays.
- (3) *Double ratios of isotopic yields.* This method uses the yields of different light isotopes produced by the system. It was developed in the grand-canonical approach, and is valid for systems at densities low enough to make fragment nuclear interaction negligible, thus the composition of the system is frozen [172]. The basic assumption is that free nucleons and fragments are in thermal equilibrium within an interaction volume V . The density of an isotope reads: $\rho(A, Z) = N(A, Z)/V = A^{3/2}\omega(A, Z)\lambda_{T_N}^{-3} \exp(\mu(A, Z)/T)$, where ω is the internal partition function of particle (A, Z) , μ its chemical potential and λ the thermal nucleon wave length. The condition of chemical equilibrium allows to define the chemical potential of a species in terms of those of free neutrons and protons and of its binding energy. Using two sets of two nuclei differing only by one nucleon, the temperature is derived from the double yield ratio, the binding energy differences and the partition functions only, the other terms disappear. The results depend on the validity of the assumptions: is the grandcanonical ensemble relevant in the studied case? Is the system really in thermal and chemical equilibrium? The considered particles should be present at freeze-out, and not produced by secondary decays. Another problem lies in the calculation of the binding energies which might depend on density and temperature. Different corrections were proposed to account for finite-size effects [173] or secondary decays [174, 175].
- (4) *Isospin thermometer approach.* At relativistic energies, it was proposed to derive the temperature at freeze-out from the isotopic distributions of the final residues [176]. The assumptions are that the fragments at freeze-out have the same N/Z ratio as the projectile; their thermal energy is dissipated through an evaporation cascade, which is reconstructed with the help of evaporation codes. The results thus entirely rely on the reliability of these codes.

A recent study on the reliability of temperature measurements for Xe QPs from Xe+Sn collisions at various energies shows that, whatever the method used, temperatures are determined at best within 10-20% [159].

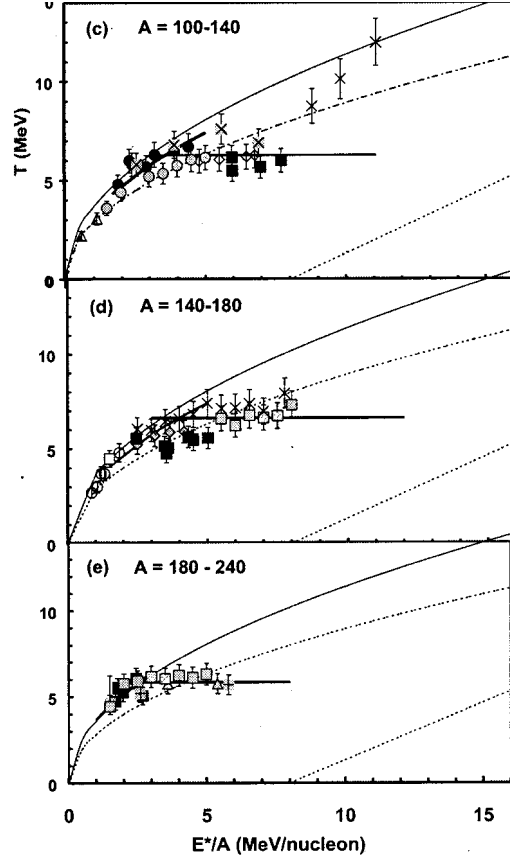


Fig. 27. Caloric curves for three selected regions of mass. The initial temperatures are plotted vs the thermal excitation energies of the systems. (Adapted from [177]).

6.3 Caloric curves

The combined and independent determinations of the thermal excitation energy and of the temperature of a system allow to draw the caloric curve, which gives the relation between these variables. The first example of caloric curve was given in [178] and taken as the evidence of the occurrence of a liquid-gas type phase transition. Many data followed, which were compiled in [177], from which is extracted fig. 27. Care was taken to recover the initial temperature of the systems by applying corrections, as mentioned in sect. 6.2, to account for the deexcitation cascade, or with the help of a statistical model. The published excitation energies were considered as pure thermal energy, except in the case of a heavy ion reaction for which the thermal part was evaluated with the SMM model. The general trend of these curves, classified in different mass zones, is first the well-known rising part attributed to the Fermi gas ($E^* = aT^2$, with a the level density parameter), followed by a plateau. The temperature at the plateau, as well as the energy at which it is first reached, were seen to decrease for larger masses. This reminded of the evolution of the

predicted limiting temperatures caused by Coulomb instabilities [179, 180]. More recently, caloric curves were published which use the temperatures obtained from hard thermal photon spectra [171, 181]. The results do not clearly exhibit a plateau, but above 3-4 MeV/nucleon of excitation the caloric curves fall below that expected for the Fermi gas. Finally a theoretical study in the microcanonical framework of the MMM model calibrated the different isotopic temperatures against the true microcanonical one [173]: the authors found a universal relation for all masses, and used it to re-evaluate some published caloric curves. The corrected curves all exhibit three parts, the Fermi gas one, a more or less broad plateau followed by a linearly rising part attributed to a “classical” gas region. Further discussion on caloric curves will be presented in sect. 8 in relation with phase transitions.

7 Freeze-out properties

The concept of freeze-out was first introduced as a starting point in statistical models. It can be defined as a configuration for which mutual nuclear interactions between primary products of a multifragmenting source become negligible. Moreover, for the sake of simplicity, those products are supposed to be spherical and having eventually recovered normal density. It was shown recently, using dynamical simulations as BOB, that such a simple geometrical picture can be relevant on the event by event basis [182]. *The freeze-out configuration characterizes the new physical state produced by the excited finite system.* In particular the freeze-out volume appears as a key quantity and its knowledge is particularly important in the extraction of thermostatics observables as the microcanonical heat capacity (see section 8). Relative velocity correlations including fragments and particles as well as different types of simulations compared to data have been used to progress with the difficult task of determining the freeze-out volume.

7.1 Fragment velocity correlations and event topology at freeze-out

Fragment-fragment relative velocity correlations functions were widely used in the 90’s to derive information on emission time scales and the disassembling source volume. Most of the papers published on the subject make use of the formalism developed in [183], where arguments are presented which justify a classical treatment of such correlations. The importance of Coulomb effects and momentum conservation laws is underlined. In this picture, it is suggested to mix correlations obtained with fragments of different sizes by replacing the relative velocity, v_{rel} , between two fragments of charge Z_i and Z_j by a reduced velocity, $v_{red} = v_{rel}/\sqrt{Z_i + Z_j}$; in this formula the mass of

the fragments is supposed to be twice their charge, meaning that it is more appropriate for light fragments. The uncorrelated yield necessary to build the correlation function was generally obtained from event mixing between events of the same class [184, 185]. As for particle-particle correlations, one obtains information on the space-time extent of the emitting source. A majority of the results deal with trajectory calculations, assuming an exponential probability distribution of the time delay between emitted fragments, $P(t) \propto \exp -t/\tau$. Excitation functions show that, for central collisions, the space-time extent decreases when the bombarding energy is raised: times around 300-500 fm/c are reported around 30 MeV/nucleon, while they are between 50 and 100 fm/c above 60 MeV/nucleon [186, 187]. For multifragmenting quasi-projectiles produced in semi-peripheral collisions, fragment emission times of 200-500 fm/c are reported in [188], for the Cu+Au reaction at 50 MeV/nucleon, independently of the assumed volume of the QP source; for Ni QP from the Ni+Au reaction at 34.5 MeV/nucleon, τ decreases from 550 to 75 fm/c when the excitation energy increases from 2 to 7 MeV/nucleon and remains constant beyond [189]. Thus on average, QP fragment emission times are comparable to those of central collisions, as appears in fig. 3, where the emission times are plotted versus the source excitation energy. Finally velocity correlations were also studied in hadron-nucleus reactions as a function of the excitation energy deposited in the nucleus [98]. Emission times were shown to decrease from $\tau=500$ fm/c at $E^*/A=2$ MeV to $\tau \sim 20-50$ fm/c for $E^*/A \geq 5$ MeV. The time range quoted at high excitation accounts for corresponding associated volumes 6-4 V_0 . Figure 3 shows that the times obtained for these reactions are systematically shorter than those measured in nucleus-nucleus collisions, by a factor of about 5. The authors of [98] tentatively explain this observation by a better source selection in hadron-induced reactions. This would act on the excitation energy axis only (through the energy range of included lcp, the collective energies). Altogether, these results testify for an increased thermal energy deposition in collisions when raising the excitation energy.

In a few cases, fragment-fragment velocity correlation functions were compared to a full calculation coupling a dynamical simulation of the collision to an after-burner. Phase-space coordinates of the fragments produced in the first phase are injected in the second one. Two examples will be given here, one coupling QMD and SMM for central 100 MeV/nucleon Fe+Au collisions [190], and the other using the stochastic mean field BOB simulation followed by the SIMON deexcitation for central 32 MeV/nucleon Xe+Sn and 36 MeV/nucleon Gd+U reactions [78]. Provided that the models accounts sufficiently well for more simple fragment properties, which was verified in both cases, a good reproduction of the correlation functions (filtered by the experimental apparatus) allows to trust the freeze-out volume and the multifragmentation time given by the dynamics. For the Fe+Au reaction, thermal multifragmentation of the quasi-target was shown to be the dominant mechanism. The freeze-out volume is given by the SMM parameter κ . The overall agreement between data and calculations is not very good (fig. 28 left), nevertheless the rising

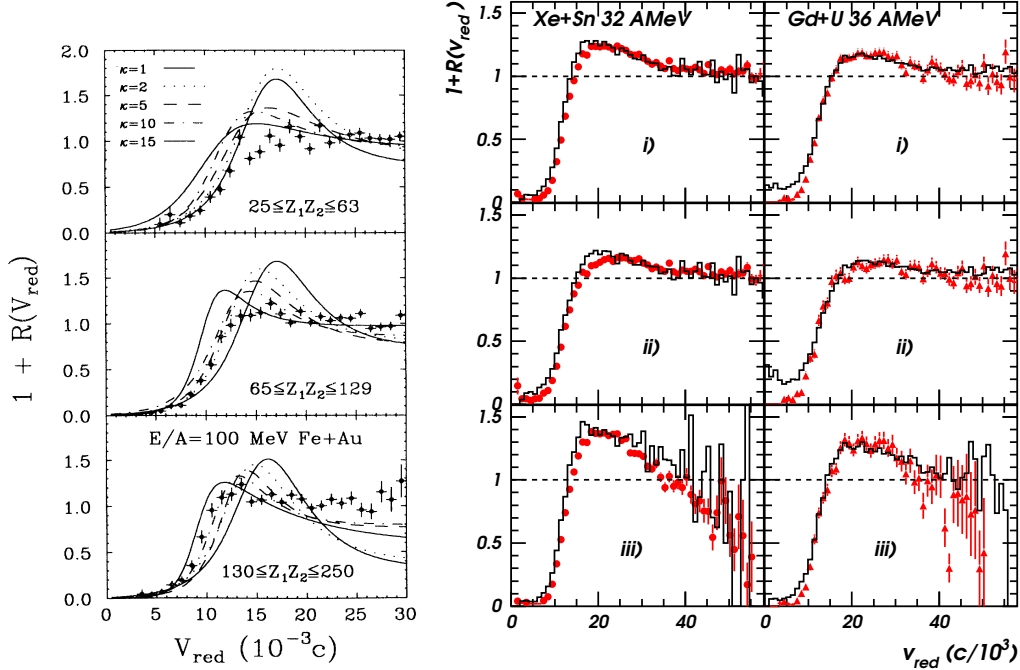


Fig. 28. Experimental reduced velocity correlation functions (symbols) for central collisions in the reactions Fe+Au (left [190]) and Xe+Sn and Gd+U(right [78]) for different charges of the fragment pairs. The lines represent calculations from QMD+SMM and different freeze-out volumes in the left panel, and from BOB in the right panel. See text for details

part after the Coulomb hole allows to derive freeze-out volumes which increase between 2 and $10V_0$ (or alternatively shorter emission times) with the charge of the fragment pair. Times shorter than $500 \text{ fm}/c$ are indicated. That small fragments are emitted from a hotter and more dense source was also suggested in [191] from large angle correlation results. In the case of reactions between heavier ions near the Fermi energy, where the formation of compact single sources was evidenced, the BOB+SIMON model well reproduces the three types of pair selections, with no cuts on the fragment energy/velocity:

- i) all fragments considered ($Z_{i,j} \geq 5$);
- ii) intermediate mass fragments (IMF) $5 \leq Z_{i,j} \leq 20$;
- iii) reduced velocity correlation of the heaviest fragment Z_{max} with each of the others in the event $Z_i < Z_{max}$.

Note that Li and Be are not considered in that case. The almost perfect matching of the calculated correlation functions with the data, particularly for Gd+U (fig. 28 right), led the authors of ref [78] to extract average freeze-out volumes (with a definition close to the SMM one) around $4V_0$ for Xe+Sn and $8V_0$ for Gd+U. The freeze-out instant was defined as that when the average fragment multiplicity becomes frozen [182], namely 200 (240) fm/c after the incident partners come to contact for Xe+Sn (Gd+U). The freeze-out topologies found in the simulations imply that the heavier fragments are located closer to the center, as shown in fig. 29. Note that in ^3He induced re-

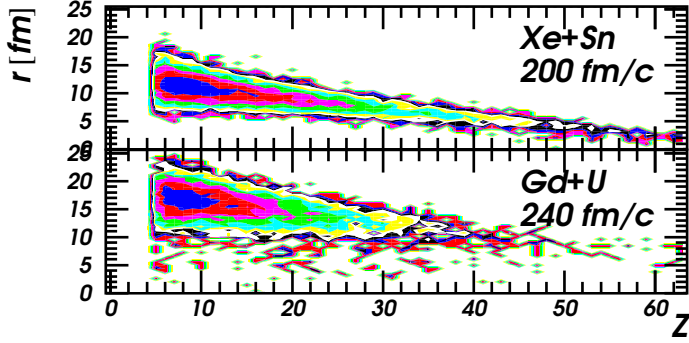


Fig. 29. Fragment positions as a function of the atomic number at the freeze-out instant for 32 MeV/nucleon $^{129}\text{Xe}+^{119}\text{Sn}$ - upper panel, and 36 MeV/nucleon $^{155}\text{Gd}+^{238}\text{U}$ - lower panel. The contour scale is logarithmic. Adapted from [78]

actions it was conversely found that the heavier fragment should be randomly positioned in a dilute source in order to well account for the experimental correlation functions with a trajectory calculation[191]. This observation may sign a difference in the fragmentation process whether it is thermally driven as it seems for QP and hadron induced reactions or it follows a compression phase as in very heavy-ion central collisions. In that case self similar expansion should favour coalescence of primary fragments close to the centre of mass.

7.2 Fragment-particle correlations and fragment excitation at freeze-out

Excitation energy measurements of primary fragments which are present at the freeze-out stage are also of large interest. They can provide information on the degree of equilibration at freeze-out and put strong constraints on freeze-out characteristics through a microcanonical description of multifragmentation events. Such measurements are derived from fragment-particle correlations. By using the correlation technique for the relative velocity between light charged particles and fragments, one can extract the multiplicities and average kinetic energies of particles emitted by fragments with a given final charge, and then reconstruct the sizes and excitation energies of the primary fragments. This technique, first proposed in [192] for Xn+Sn central collisions at 50 MeV/nucleon incident energy, was applied from 32 to 50 MeV/nucleon [193] and for Kr+Nb central collisions at 45 MeV/nucleon [194]. For each bombarding energy, a constant value of the mean excitation energy per nucleon has been found over a primary fragment charge range 5-20, which strongly suggests that fragments are on average in thermal equilibrium at freeze-out. This average excitation energy, equal to 2.2 MeV/nucleon at the lower incident energy, saturates around 2.5-3.5 MeV/nucleon for beam energies 39 MeV/nucleon and above. Note that dynamical simulations (AMD, BOB) performed for Xe+Sn central collisions at similar incident energies [77, 91] predict average values

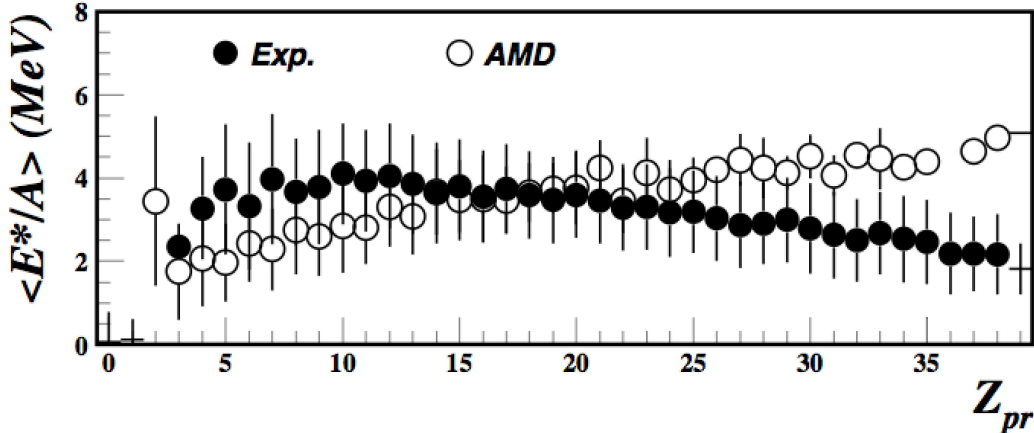


Fig. 30. Average excitation energy of primary fragments as a function of the atomic number for 50 MeV/nucleon Xe+Sn central collisions. Full points refer to experimental evaluations using fragment-particle correlations and open points to AMD simulations. From [77]

close to 3 MeV/nucleon for fragment excitation at freeze-out. However a detailed comparison between data and AMD simulations, displayed in fig. 30, shows different evolutions with fragment charge; the increase of the fragment excitation energy per nucleon with its charge is a general trend of AMD results in the Fermi energy region (see also [81]). Going more into the details of correlation results, one learns that the corresponding secondary evaporated light charged particles represent less than 40% of all produced charged particles and decreases down to 20% for 45-50 MeV/nucleon incident energies. Finally experimental data are better reproduced with secondary deexcitation simulations assuming that the fragment N/Z ratio at freeze-out is the same as that for the combined projectile-target system.

7.3 Break-up densities and freeze-out volumes

From an experimental point of view the location of nuclear multifragmentation data in the phase diagram requires accurate independent measurements of temperature and density at the break-up stage. While the problem of temperature has been solved with acceptable accuracy using He-Li isotope ratios up to 5-6 MeV [15], no accurate enough method is available to determine the spatial extension of mononuclear systems which undergo multifragmentation. Therefore estimates of break-up densities have been obtained using various approaches. For instance, break-up densities for spectator fragmentation in Au+Au collisions at 1000 MeV/nucleon were estimated by using selected particle-particle correlations (particles from secondary decays are excluded by imposing an energy threshold) [195]. Assuming a zero lifetime, the volumes of spectator sources were extracted and densities calculated by dividing the

number of spectator constituents by the source volume. The estimated average values slowly decrease from about 0.3 to 0.2 ρ_0 when excitation energies of spectators move from 4 to 10 MeV/nucleon. Caloric curves were analyzed within the framework of an expanding Fermi gas hypothesis to extract estimates of break-up densities [196]. In this approach the observed flattening of the caloric curves reflects an increasing expansion with increasing excitation energy (the product $Tx\rho^{-2/3}$ is a constant within a isentropic hypothesis). For nuclei of medium to heavy mass, the derived density values vary from 0.7-0.6 to 0.4 ρ_0 when excitation energies increase from 4 to 6-8 MeV/nucleon. Starting from the definition of freeze-out given at the beginning of that section, one can compare break-up density/volume to freeze-out volume obtained from dynamical simulations as BOB. Taking the case of Xe+Sn central collisions at 32 MeV/nucleon (source excitation energy close to 6 MeV/nucleon), break-up density coming from simulations is $0.41\rho_0$ or $2.4V_0$ and the corresponding average freeze-out volume $V_{F.O.}^{SMM}$ is $2.8V_0$ with the definition of SMM (which corresponds to a sphere including all the centres of primary fragments) and $6.1V_0$ for $V_{F.O.}^{sph.}$ a sphere including all fragments [78, 197]. As we see $V_{F.O.}^{SMM}$ well compares, at least for that system size, to the break-up volume.

Average freeze-out volumes have been extracted first from comparisons with statistical models like SMM as shown for some examples in subsection 5.2. In general, experimental results can be well reproduced over a large range of excitation energy (from 2 to 10, 12 MeV/nucleon), by keeping the same $V_{F.O.}^{SMM}$ typically 3 or $6V_0$. Recently a first attempt of estimating the freeze-out volume in a fully consistent way was done, by employing a simulation built event by event from all the available asymptotic experimental information (charged particle spectra, average and standard deviation of fragment velocity spectra and calorimetry) [198]. Dressed excited fragments, which statistically deexcite, and particles at freeze-out are described by spheres at normal density. Four free parameters are used to recover the data: the percentage of measured particles which were evaporated from primary fragments, the collective radial energy, a minimum distance between the surfaces of products at freeze-out and a limiting temperature for fragments (see [198] for more details). For Xe+Sn data (32 MeV/nucleon, central collisions) an average volume $V_{F.O.}^{sph.} = 7.6 \pm 2.0V_0$ was derived. However the deduced average excitation energy for primary fragments is close to 4 MeV/nucleon, significantly higher than the value of 2.2 MeV/nucleon evaluated from fragment-particle correlations (see previous subsection). Note that the use of the widths of fragment velocity spectra in the comparison between data and simulation has shown that the introduction of a limiting temperature for fragments seems mandatory. The strong sensitivity of the freeze-out volume to limiting temperature values was also demonstrated in the microcanonical multifragmentation model MMM as far as average properties of fragments are used to put constraints on volumes [199].

In conclusion we can say that working hypotheses and approximations are used to give semi-quantitative information on average break-up densities or

freeze-out volumes. Values remaining constant around $0.2-0.3\rho_0$ or slowly decreasing from 0.6 to $0.3\rho_0$ over the excitation energy range $3-12$ MeV/nucleon are derived. The restoration of freeze-out stage using all the asymptotic experimental information appears as promising.

8 Finite systems and phase transitions

Phase transitions are universal properties of interacting matter and traditionally they have been studied in the thermodynamical limit of infinite systems. A phase transition occurs when a phase becomes unstable in given thermodynamical conditions described with intensive variables like temperature, pressure However in physical situations, as the one encountered in the present studies concerning isolated finite systems like nuclei, the concept of thermodynamical limit can not apply. Extensive variables like energy and entropy are no more additive due to the important role played by the surfaces of particles and fragments which are produced. The entropy of the surfaces which separate the coexisting phases does not scale with the size of the system. The entropy per particle at equilibrium $s=S(E)/N$ shows a convexity with a depth proportional to $N^{-1/3}$ which is suppressed at the thermodynamical limit. Consequently phase transitions should be reconsidered from a more general point of view. An important theoretical effort started a few years ago to propose and discuss signatures of phase transitions in small systems [137, 200, 201, 202, 203, 204, 205, 206, 207, 208, 209, 210, 211, 212, 213, 214, 215, 216, 217, 218, 219, 220, 221, 222, 223, 224, 225, 226, 227]. “Small” systems have been defined in reference [205] as systems where the linear dimension is of the same order of magnitude as the characteristic range of the interaction. This is for example the case for atomic clusters but also for astrophysical systems, due to the long range of gravitation. Such systems are also classified as non-extensive systems.

This section is divided into three parts. One is devoted to the possible dynamics of phase transition for hot unstable nuclei. In a second part we shall discuss the thermostatics involved and the associated relevant signatures. Finally critical behaviours early observed in multifragmentation data will be discussed in the context of finite systems.

8.1 Dynamics and spinodal instability

We have noticed in previous sections experimental evidence for a radial extra energy boost (radial expansion energy) associated to multifragmentation products. It can be attributed either to a dominant compression-expansion phase in central nucleus-nucleus collisions or to thermal pressure for more

gentle collisions: hadron-nucleus or semi-peripheral nucleus-nucleus collisions. The system might then reach densities and temperatures that correspond to spinodal instability and clusterization would ensue as the system seeks to separate into the corresponding coexisting liquid and gas phases.

In the last fifteen years major theoretical progresses have been realized to understand and learn about spinodal decomposition in the nuclear context and a review can be found in reference [220]. We shall first briefly discuss what are the specificities of spinodal decomposition as far as infinite nuclear matter is concerned. Associated to negative compressibility the mechanically unsta-

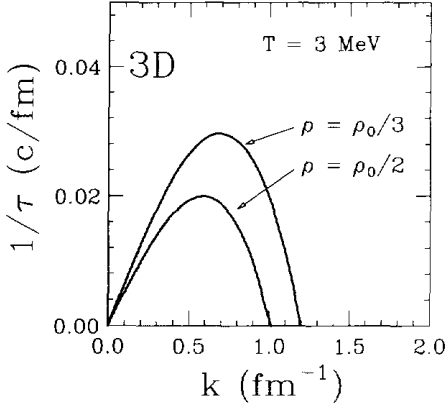


Fig. 31. Nuclear matter dispersion relation at 3 MeV temperature for two different densities; ρ_0 is the normal density. (from [228]).

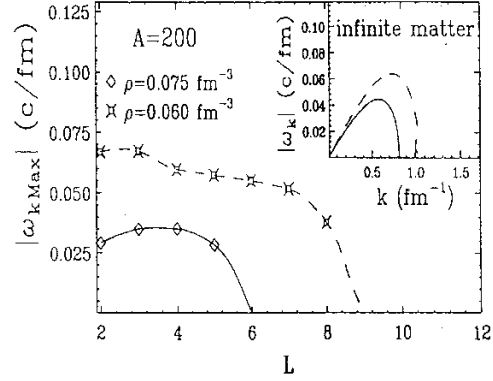


Fig. 32. Growth rates of the most unstable modes for a spherical source with 200 nucleons as a function of the multipolarity L and for two different central densities. (from [229]).

ble spinodal region can be investigated by studying the propagation of small density fluctuations [228, 230]. By analogy with optics, the nuclear dispersion relation can be calculated for different conditions of temperature and density by introducing the Boltzmann-Langevin equation (see subsection 5.3.2). Within the linear response theory framework, if one expands the solution of the Boltzmann-Langevin equation as $f = f_0 + \delta f$, where f_0 is a solution of the Boltzmann equation and δf the fluctuating part, one finds the equation of motion $\partial \delta f / \partial t = -i \mathcal{M} \delta f + \delta I[f_0]$ at the leading order in δf . The extended RPA matrix \mathcal{M} represents the combined action of the effective field and of the average collision term. In the spinodal region the eigenvalues of the matrix \mathcal{M} become imaginary. Consequently the fluctuations associated with a given eigenmode agitated by the source term δI are exponentially amplified or suppressed, depending upon the sign of the imaginary part of the frequency. In the case of infinite nuclear matter the eigenmodes of the linearized dynamics are plane waves, characterized by a wave number k and an imaginary eigenfrequency, which is the inverse of the instability growth time. Figure 31 presents an example of nuclear dispersion relation at 3 MeV temperature for two different densities $\rho_0/2$ and $\rho_0/3$. Imaginary RPA frequencies are reported as a

function of the wavenumber k of the considered perturbation. This dispersion relation exhibits a strong maximum at a given wave number followed by a cut-off at large k values. This cut-off reflects the fact that fluctuations with wavelength smaller than the range of the force can not be amplified. The most unstable modes correspond to wavelengths lying around $\lambda \approx 10$ fm and the associated characteristic times are almost identical, around 30-50 fm/c, depending on density ($\rho_0/2$ - $\rho_0/8$) and temperature (0-9 MeV) [228, 231]. A direct consequence of the dispersion relation is the production of “primitive” fragments with size $\lambda/2 \approx 5$ fm which correspond to $Z \approx 10$. However this simple and rather academic picture is expected to be largely blurred by several effects. We do not have a single unstable mode and consequently the beating of different modes occurs. Coalescence effects due to the residual interaction between fragments before the complete disassembly are also expected [228] and finally primary fragments deexcite by secondary decay.

Does the signal discussed for nuclear matter survive (in final fragment partitions experimentally measured) if we consider the case of a hot expanding nucleus which undergoes multifragmentation? First of all, the system produced by the collision has to stay long enough in the spinodal region (≈ 3 characteristic time: 100-150 fm/c) to allow an important amplification of the initial fluctuations. Secondly, the presence of a surface introduces an explicit breaking of the translational symmetry. Figure 32 shows the growth rates of the most unstable modes for a spherical source of $A=200$ with a Fermi shape profile and for two different central densities [229]. The growth rates are nearly the same for different multiplicities L up to a maximum multiplicity L_{max} (see also [232]). This result indicates that the unstable finite system breaks into different channels. Depending on multiplicity L , equal-sized “primitive” fragments are expected to be produced with sizes in the range $A_F/2$ - A_F/L_{max} ; A_F being the part of the system leading to fragments during the spinodal decomposition. One can also note that the Coulomb potential has a very small effect on the growth rates of unstable collective modes except close to the border of the spinodal zone where it stabilizes very long wave-length unstable modes [233]. On the other hand, for a finite system, Coulomb interaction reduces the freeze-out time and enhances the chance to keep a memory of the dynamical instabilities; a similar comment can be made as far as collective expansion is concerned. Both effects push away the “primitive” fragments and reduce the time of their mutual interaction. So finally, even if expected strongly reduced, the presence of partitions with nearly equal-sized fragments is a good candidate to sign the role of spinodal instability in multifragmentation.

Following early studies related to nearly equal-sized fragment partitions [234], ten years ago a method called higher order charge correlations [235] was proposed to enlighten any extra production of events with specific fragment partitions. The high sensitivity of the method makes it particularly appropriate to look for small numbers of events, as those expected to have kept a memory of spinodal decomposition properties. Thus the charge correlation method

allows to examine model independent signatures that would indicate a preferred decay into a number of equal-sized fragments in events from experimental data or from simulations. All fragments of one event with fragment multiplicity $M_f = M = \sum_Z n_Z$, where n_Z is the number of fragments with charge Z in the partition, are taken into account. By means of the normalized first, $\langle Z \rangle$, and second order, σ_Z^2 , moments of the fragment charge distribution in the event, one may define the higher order charge correlation function as: $1 + R(\sigma_Z, \langle Z \rangle) = (Y(\sigma_Z, \langle Z \rangle)/Y'(\sigma_Z, \langle Z \rangle))|_M$. Here, the numerator $Y(\sigma_Z, \langle Z \rangle)$ is the yield of events with given $\langle Z \rangle$ and σ_Z values. The denominator $Y'(\sigma_Z, \langle Z \rangle)$, which represents the uncorrelated yield of pseudo-events, can be built in different ways; details and discussions can be found in [72, 236, 237]. The exact identification of fragments up to at least $Z=20$ is mandatory to use that method. It was applied on different data sets corresponding to com-

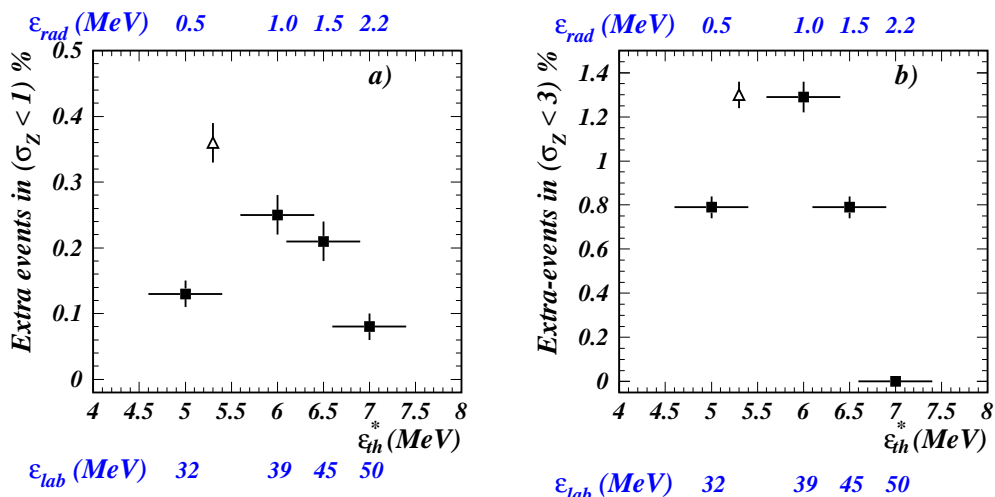


Fig. 33. Extra production of events with nearly equal-sized fragments (a: $\sigma_Z < 1$ and b: $\sigma_Z < 3$) as a function of thermal excitation energy (full points); the incident and radial energy scales are also indicated. ϵ_{th}^* and ϵ_{rad} are deduced from comparisons with SMM. The open point refers to the result from BOB simulations; the average thermal excitation energy is used. Vertical bars correspond to statistical errors and horizontal bars refer to estimated uncertainties on the backtraced quantity, ϵ_{th}^* . (from[72]).

pact single sources produced in central collisions in the incident energy range 30-50 MeV/nucleon [237]. For the $^{129}\text{Xe} + \text{nat}\text{Sn}$ system [72, 238] a rise and fall of the percentage of extra production of events with nearly equal-sized fragments was observed. The average-charge domains contributing to the correlation peaks are 12-21 and come mainly, as theoretically expected, from fragment multiplicity 3 (dominance of the octupole mode) [239]. Figure 33 illustrates the results for two different limits on σ_Z ; the lower limit corresponds to the spread estimated as coming from secondary fragment evaporation and the higher limit to the observed spread for the correlation function. Results obtained with BOB simulations (see section 5) are also reported. For the con-

sidered system, incident energies around 35-40 MeV/nucleon appear as the most favourable to induce spinodal decomposition; it corresponds to about 5.5-6 MeV/nucleon thermal excitation energy associated to a very gentle expansion energy around 0.5-1 MeV/nucleon. The qualitative explanation for those numbers can be well understood in terms of a necessary compromise between two time scales. On one hand the fused systems have to stay in the spinodal region ≈ 100 -150 fm/c [228, 231, 240], to allow an important amplification of the initial fluctuations and thus permit spinodal decomposition; this requires a not too high incident energy, high enough however for multifragmentation to occur. On the other hand, for a finite system, Coulomb interaction and collective expansion push the “primitive” fragments apart and reduce the time of their mutual interaction, which is efficient to keep a memory of “primitive” size properties.

At present confidence levels around 3-4 σ , observed for charge correlation peaks, prevent any definitive conclusion. To firmly assess or not the validity of this fossil signal new experiments with higher statistics are required.

If this fossil signal is definitively confirmed the following comments have to be done. As we have shown in fig. 21, good average statistical descriptions of data using for example SMM are also obtained, which could demonstrate that the dynamics involved for finite systems is sufficiently chaotic to finally explore enough of the phase space in order to describe fragment production through a statistical approach. It is tempting to associate a part of that chaos with the coalescence stage which can occur during fragment formation. Indeed, as shown previously (sections 4 and 7), the peculiar size and position of the largest fragment could be well understood as resulting from mode beating (size), large-wavelength instabilities (size) and the late-stage coalescence related to the involved bulk nuclear density (size and position).

8.2 *Spinodal instability and Thermostatistics*

Spinodal instability is intimately related to the occurrence of a first order phase transition as signaled by a convex anomaly in the entropy function $S(X)$. For pedagogical purpose we consider in the following only one single extensive variable X like energy, volume or number of particles. Entropy can be gained by separating the uniform system into two phases at equilibrium: it is the spinodal decomposition well known at the thermodynamical limit for binary solutions and binary alloys. Figure 34 illustrates the relationship between entropy convexity, spinodal instability and phase coexistence. Two signatures of a phase transition for hot nuclei can be added to the previous one (observation of nearly equal-sized fragments), just starting from the fact that surfaces are no more negligible for finite systems. The entropy of the combined system constituted by the two coexisting phases is not a sum of the individual subsystem entropies. The uniform unstable finite system gains entropy by re-

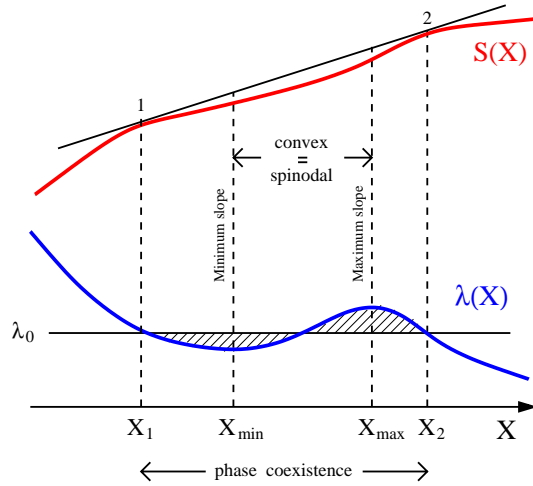


Fig. 34. Phase coexistence and spinodal instability. The entropy function $S(X)$ is convex between the inflection points X_{min} and X_{max} where the intensive conjugate variable $\lambda(X)=\delta(S)/\delta(X)$ has a local minimum or maximum, respectively. The infinite system is mechanically unstable and entropy is gained by separating the system into two phases. The entropy of the corresponding mixed system is additive and moves along the common tangent as X increases from X_1 to X_2 ; the intensive conjugate variable is determined by the Maxwell construction requiring that the two hatched areas are equal.(from [220]).

organizing itself into a mixture of the two phases but the resulting equilibrium entropy function keeps a local convexity. The Maxwell construction is no more valid as illustrated in fig. 35.

The two main consequences of that local convexity are the following. Using a microcanonical sampling (fixed values of the extensive variable E which can be rather well estimated from experiments) the first derivative corresponds to the inverse microcanonical temperature and the bottom curve of fig. 34 is the inverse of a caloric curve which presents a backbending. The energetic cost paid to produce surfaces is a decrease of the microcanonical temperature when the excitation energy increases and consequently the appearance of a negative microcanonical heat capacity [200, 202] as a specific signature of a first order phase transition for finite systems. Moreover if a signature of spinodal instability is observed one must measure correlatively a negative microcanonical heat capacity related to the resulting equilibrium entropy function with local convexity. The reverse is not true if spinodal instabilities are not responsible for fragment formation. Experimental observations of correlated signals will be discussed in the next section.

If one considers now a finite system in contact with a reservoir (canonical sampling), the value of X may fluctuate as the system explores the phase space; the associated distribution at equilibrium is $P(X)\sim\exp(S(X)-\lambda X)$. The distribution of X acquires a bimodal character (see fig. 36): that bimodality is a second specific signature of a first order phase transition for finite systems.

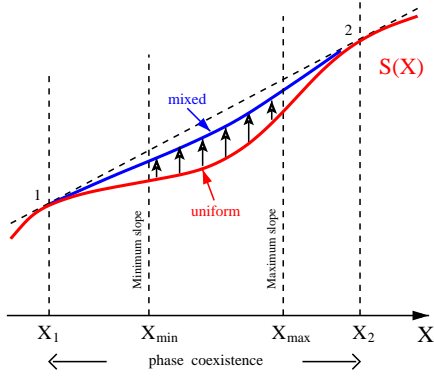


Fig. 35. Isolated finite systems. The entropy function for a uniform unstable system (lower curve) has a local convexity region and the system gains entropy reorganizing itself into a mixture of the two phases. The resulting equilibrium entropy function (upper curve) will always lie below the common tangent (dashed line) (from [220]).

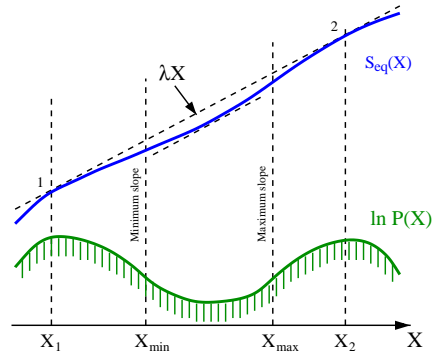


Fig. 36. Canonical ensemble of finite systems. The bimodal equilibrium distribution is given by $P(X) \sim \exp(S(X) - \lambda X)$. The figure shows the case when the Lagrange multiplier λ is equal to the slope of the common tangent (from [220]).

It gives an understanding of coexistence as a bimodality of the event distribution, each component being a phase. We recall that for infinite systems two delta function distributions are localized in X_1 and X_2 and correspond to spinodal decomposition. The biggest fragment detected in each multifragmentation event, because of its correlation with the density which is the natural order parameter of the liquid-gas phase transition, is a good candidate as a potential order parameter. A priori that second specific signature can be directly observed from experiments and could appear as robust. A difficulty comes however from the absence of a true canonical sorting in the data. The statistical ensembles produced by selecting for example fused systems are neither canonical nor microcanonical and should be better described in terms of the Gaussian ensemble [241], which gives a continuous interpolation between canonical and microcanonical ensembles. Very recently a simple reweighting of the probabilities associated to each excitation energy bin for quasi-projectile events was proposed to allow the comparison with the canonical ensemble [242]. Signals of bimodality will be discussed and correlated to other signals in the next section. *Finally one can also underline a very important consequence of bimodality: for finite systems large fluctuations of “order parameters” are expected to be observed in the middle of the coexistence region.*

8.2.1 Caloric curves, negative microcanonical heat capacity and abnormal energy fluctuations

The observation of a plateau in nuclear caloric curves was experimentally proposed as a direct signature of a first-order phase transition [178]. However, from a theoretical point of view, a plateau-like shape can not be an unambiguous signature even if it is a strong indication of a physical change and if its observation can help to better define the energy domain of interest for phase transition. Caloric curves for restricted mass regions are presented in fig. 27. Indeed measured caloric curves can be misleading because different curve shapes can be generated depending on the path followed in the microcanonical equation of state surface. As examples calculated caloric curves (microcanonical lattice gas model-216 particles) at a constant pressure or a constant average volume [137] are displayed in the upper part of fig. 37. At constant pressure a backbending is clearly seen whereas at constant average volume a smooth behaviour is observed showing that the phase transition signal can be hidden in the observation of caloric curves. In experiments one does not explore a caloric curve at constant pressure nor at constant volume, the system follows a path in the excitation energy freeze-out volume plane. For

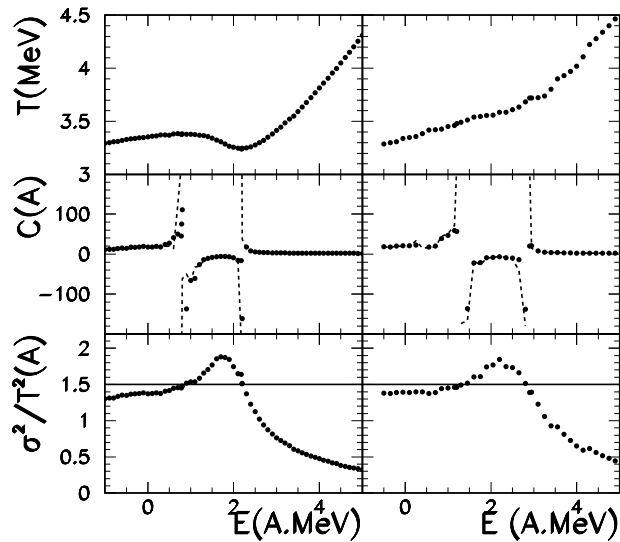


Fig. 37. Thermodynamic quantities in the microcanonical ensemble for a transformation at constant pressure (left part) and at constant volume (right part). Caloric curves are displayed in upper panels. Normalized kinetic energy fluctuations are compared to the canonical expectation (lines) in lower panels. In medium panels microcanonical heat capacities (symbols) are compared to the estimation (dashed lines) discussed in the text. (from [137]).

overcoming that situation it was proposed to directly measure the heat capacity; if an experimental path is intersecting the spinodal region of the system phase diagram, it would be signaled by a negative value of the microcanonical

heat capacity. A method for measuring microcanonical heat capacity using partial energy fluctuations was proposed [137, 204, 243]. Abnormal partial energy fluctuations (as compared to the canonical expectation) are indeed always seen, independently of the path, if microcanonical negative heat capacity is present. The prescription is based on the fact that for a given total energy of a system, the average partial energy stored in a part of the system is a good microcanonical thermometer, while the associated fluctuations can be used to construct the heat capacity. From experiments the most simple decomposition of the total energy E^* is in a kinetic part, E_k , and a potential part, E_p , (Coulomb energy + total mass excess). However these quantities have to be determined at freeze-out and consequently it is necessary to trace back this configuration on an event by event basis. As discussed in the previous section the fragment properties entirely rely on the representation of the system at the freeze out stage as non interacting fragments. The true configuration needs the knowledge of the freeze-out volume and of all the particles evaporated from primary hot fragments including the (undetected) neutrons. Consequently some working hypotheses are used, possibly constrained by specific experimental results [244]. Then, the experimental correlation between the kinetic energy per nucleon E_k/A and the total excitation energy per nucleon E^*/A of the considered system can be obtained as well as the variance of the kinetic energy σ_k^2 . Note that E_k is calculated by subtracting the potential part E_p from the total energy E^* and consequently kinetic energy fluctuations at freeze-out reflect the configurational energy fluctuations. An estimator of the microcanonical temperature of the system can be obtained by inverting the kinetic equation of state:

$$\langle E_k \rangle = \langle \sum_{i=1}^M a_i \rangle T^2 + \langle \frac{3}{2}(M-1) \rangle T$$

The brackets $\langle \rangle$ indicate the average on events with the same E^* , a_i is the level density parameter and M the multiplicity at freeze-out. An estimate of the total microcanonical heat capacity is extracted from the following equations:

$$C_k = \frac{\delta \langle E_k/A \rangle}{\delta T}; \quad A\sigma_k^2 \simeq T^2 \frac{C_k C_p}{C_k + C_p}; \quad \left(\frac{C}{A}\right)_{micro} \simeq C_k + C_p \simeq \frac{C_k^2}{C_k - \frac{A\sigma_k^2}{T^2}}$$

The specific microcanonical heat capacity $(C/A)_{micro}$ becomes negative if the kinetic/configurational energy fluctuations $A\sigma_k^2$ overcome $C_k T^2$. Figure 37 (medium and lower panels) illustrates the results of such a procedure in the framework of a microcanonical lattice gas model.

That procedure was applied by the MULTICS and INDRA collaborations on different sources produced in peripheral and central heavy ion collisions in the incident energy range 30-80 MeV/nucleon [158, 245, 246, 247, 248, 249, 250]. Figure 38 summarizes the results obtained by the MULTICS collaboration: on the left side it is seen that normalized kinetic energy fluctuations overcome

the estimated canonical fluctuations, C_k ; the right part of the figure illustrates the microcanonical negative heat capacities observed, the distances between the poles being associated with the latent heat.

These results provide a direct evidence of a first order liquid-gas phase transition. They have to be seen as semi-quantitative and correspond to a starting point for more precise measurements needed for the reconstruction of the phase diagram. We recall again that the present protocol of measurements is discussed in details in reference [244]. Exact microcanonical formulae, assum-

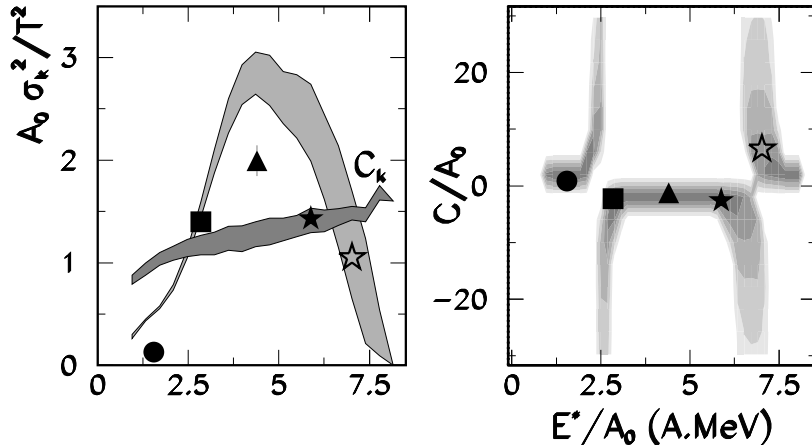


Fig. 38. Left panel: normalized kinetic energy fluctuations and estimated canonical fluctuations (C_k) for quasi-projectile (QP) events produced in Au+Au collisions at 35 MeV/nucleon (grey zones) and for fused systems produced in central Au+C (black dots), Au+Cu (squares, triangles) and Au+Au reactions before (open stars) and after subtraction of 1 MeV/nucleon radial flow (black stars). Right panel: corresponding microcanonical heat capacities per nucleon. (from [245]).

ing that a classical treatment of the motion of products emitted at freeze-out is appropriate, are also proposed in [214] to calculate heat capacity and second order derivative of the entropy versus energy. They depend on the total kinetic energy and number of emitted products which have to be estimated event by event at freeze out. However up to now this method was not used to derive information from data.

8.2.2 Microcanonical heat capacity and open questions

Before concluding on this part one can indicate that theoretical questions are still under debate and concern the topology of the system at freeze-out and the related order of the phase transition. If the system is still relatively dense at freeze-out, which seems improbable if we refer to the previous section, the fragment properties may be very different from the ones asymptotically measured and the question arises whether the energetic information measured on ground state properties can be taken for the freeze out stage [251]. Classical molecular dynamics calculations have shown that the ground state Q-value

is a very bad approximation of the interaction energy of fragments in dense systems. This is due to the deformation of fragments and to the interaction energy when fragment surfaces touch each other. As a consequence, comparable kinetic energy fluctuations are obtained in the subcritical and supercritical region of the Lennard-Jones phase diagram [223]. On the other hand calculations with a similar model, the Lattice Gas model, show that even in the supercritical region the correct fluctuation behaviour can be obtained if both the total energy and the interaction energy are consistently estimated with the same approximate algorithm as it is done in the experimental data analysis [224]. Concerning now the order of the transition, recent calculations performed within a mean-field framework (liquid drop model at finite temperature) show that the phase transition is seen to be continuous (second order) and that a negative heat capacity for finite nuclei is not incompatible with it [227].

8.3 Scaling and fluctuations for fragment sizes

In the early eighties multifragmentation was connected to a critical phenomenon [5, 252, 253, 254, 255]. Percolation models [255, 256, 257, 258], the Fisher Droplet Model [221, 226, 259, 260, 261] and more recently the theory of universal fluctuations [207, 225, 262, 263, 264] have been employed to describe fragment size distributions and fluctuations and to tentatively derive information on the critical region of the liquid-gas transition: in finite systems the critical point becomes a critical region. The determinations of a scaling function and of a consistent set of critical exponents in different multifragmentation data also tend to support this hypothesis [97, 141, 265, 266]. However the situation appeared as more complex. Indeed signals of a first order phase transition were also observed on the same set of data [97, 245, 266, 267], which opened a debate on the critical temperature extracted, on the order of the transition and on the consequences of Coulomb and finite size effects on critical behaviours [203, 268, 269, 270, 271].

8.3.1 The Fisher Droplet Model

The observation of critical behaviours like power laws in the charge/mass distribution of multifragmenting systems has been interpreted as an evidence of a second order phase transition. In the Fisher Droplet Model [259] the vapor coexisting with a liquid in the mixed phase of a liquid-gas phase transition is schematized as an ideal gas of clusters, which appears as an approximation for non ideal fluids. The model was recently applied to multifragmentation data [260] by considering all fragments but the largest as the gas phase, Z_{max} being assimilated to the liquid part. The yield of a fragment of mass A reads:

$$dN/dA = \eta(A) = q_0 A^{-\tau} \exp((A\Delta\mu(T) - c_0(T)\varepsilon A^\sigma)/T).$$

In this expression, τ and σ are universal critical exponents, $\Delta\mu$ is the difference between the liquid and actual chemical potentials, $c_0(T)\varepsilon A^\sigma$ is the surface free energy of a droplet of size A , c_0 being the zero temperature surface energy coefficient; $\varepsilon = (T_c - T)/T_c$ is the control parameter and describes the distance of the actual to the critical temperature. At the critical point $\Delta\mu = 0$ and surface energy vanishes: $\eta(A)$ follows a power law. Away from the critical point but along the coexistence line $\Delta\mu = 0$ and the cluster distribution is given by: $dN/dA = \eta(A) = q_0 A^{-\tau} \exp((-c_0(T)\varepsilon A^\sigma)/T)$.

The temperature T is determined by assuming a degenerate Fermi gas. This

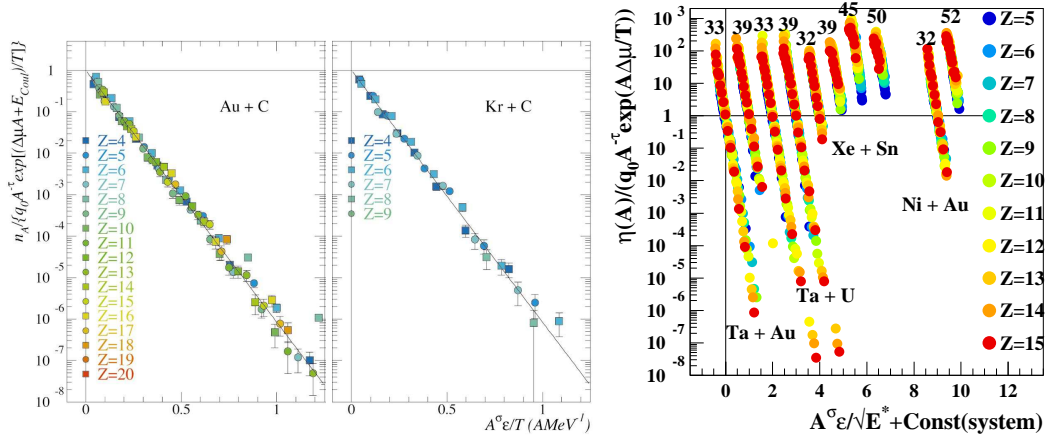


Fig. 39. Fragment mass yield distribution scaled by the power law prefactor, the chemical potential and Coulomb (added to $A\Delta\mu$ for left and central panels) terms plotted against the inverse temperature scaled by Fisher's parametrization of the surface energy. Left and central panels: data correspond to projectile fragmentation observed in reverse kinematics reactions at 1.0 GeV per nucleon, from [261]. Right panel: Data correspond to semi-peripheral (Ta+X) or central (Xe+Sn, Ni+Au) collisions. Bombarding energies in MeV/nucleon are reported on top of each scaled distribution; they are shifted by one x unit for a better view. from [267].

kind of scaling was found in many multifragmentation data, in hadron-nucleus as well as in nucleus-nucleus collisions [260, 261, 266, 267]; the agreement between data and theory often holds over orders of magnitude, and the critical exponents which are deduced are in acceptable agreement with those expected for the liquid-gas universality class. As examples, fig. 39 shows the scaling properties observed for different systems studied by the EOS and INDRA collaborations.

8.3.2 Universal fluctuations of an order parameter

The recently developed theory of universal scaling laws of order-parameter fluctuations provides methods to select order parameters, characterize critical and off-critical behaviours and determine critical point without any equilib-

rium assumption [207, 262]. In this framework, universal Δ scaling laws of one of the order parameters, m , should be observed:

$$\langle m \rangle^\Delta P(m) = \phi((m - \langle m \rangle) / \langle m \rangle^\Delta)$$

where $\langle m \rangle$ is the mean value of the distribution $P(m)$. $\Delta=1/2$ corresponds to small fluctuations, $\sigma_m^2 \sim \langle m \rangle$, and thus to an ordered phase. Conversely $\Delta=1$ occurs for the largest fluctuations nature provides, $\sigma_m^2 \sim \langle m \rangle^2$, in a disordered phase. For models of cluster production having a critical behaviour there are two possible order parameters [262]: the fragment multiplicity in a fragmentation process or the size of the largest fragment in an aggregation process (clusters are built up from smaller constituents). The method was applied

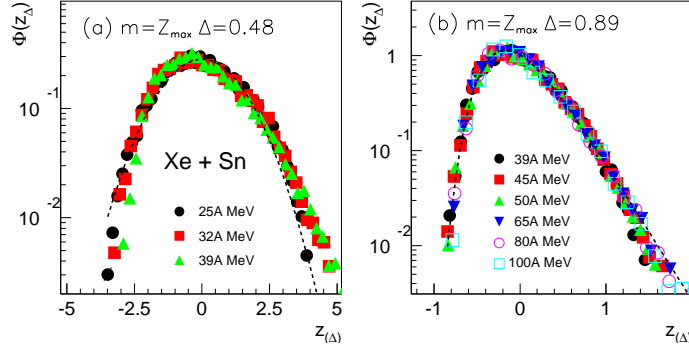


Fig. 40. (a) Z_{max} distributions for central Xe+Sn collisions at 25-39 MeV/nucleon bombarding energies, scaled according to Δ scaling equation; the dashed curve is a best fit to scaled data using a Gaussian distribution. (b) As (a) but for bombarding energies 39-100 MeV/nucleon: the dashed curve is a best fit to scaled data using the Gumbel distribution. From [264].

to central collision samples (symmetric systems with total masses ~ 73 -400 at bombarding energies between 25 and 100 MeV/nucleon) by the INDRA collaboration [263, 264]. The CP multiplicity fluctuations do not show any evolution over the whole data set. Conversely the relationship between the mean value and the fluctuation of the size of the largest fragment does change as a function of the bombarding energy: $\Delta \sim 1/2$ at low energy, and $\Delta \sim 1$ for higher bombarding energies. The form of the Z_{max} distributions also evolves with bombarding energy: it is nearly Gaussian in the $\Delta=1/2$ regime and exhibits for $\Delta=1$ an asymmetric form with a near-exponential tail for large values of the scaling variable (see fig. 40). This distribution is close to that of the modified Gumbel distribution [272], the resemblance increasing with the total mass of the system studied and being nearly perfect for the Au+Au data. The Gumbel distribution is the equivalent of the Gaussian distribution in the case of extreme values: it is obtained for an observable which is an extremum of a large number of random, uncorrelated, microscopic variables.

The dependence on bombarding energy and total system mass of the frontier between the two Δ -scalings is shown in fig. 41. Within the developed theory, this behaviour indicates the transition from an ordered phase to a disordered phase in the critical region, the fragments being produced following some ag-

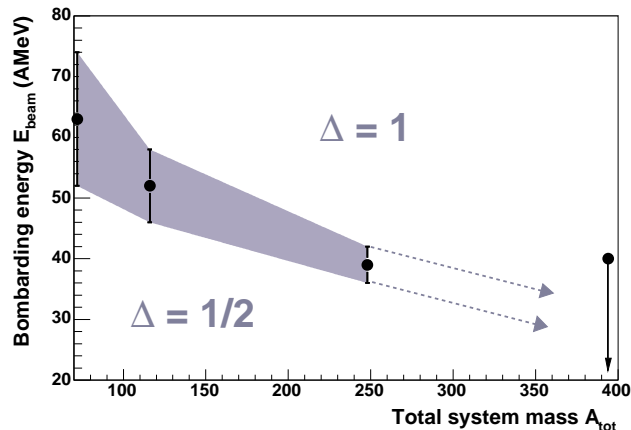


Fig. 41. Dependence on bombarding energy and total system mass of the two different regimes of Δ -scaling observed for the size of the largest fragment in each event, Z_{max} , for central collisions of symmetric systems studied with INDRA. From [264].

gregation scenario. Here again, as it was the case for the Fisher's scaling, the two Δ -scaling regimes suggest the occurrence of a second-order phase transition.

8.3.3 Finite size effects and pseudo-critical behaviours inside the coexistence region

As shown in this section, analyses of given samples of events have found at the same time scaling laws and evidence for first-order phase transition signals (negative microcanonical heat capacity and spinodal instabilities). At the thermodynamic limit, scalings are general properties of matter near the critical point and thus typical of second order phase transition. For finite systems fluctuations correlate points at a distance which can be comparable to the linear size of the system and can have an effect similar to a diverging correlation length in an infinite system. Therefore the so called critical behaviours are expected to be observed non only in the critical zone, but also deeply in the coexistence region where large fluctuations have been observed. Within a lattice gas model in the canonical ensemble a scaling behaviour, with critical parameters close to the ones expected for the liquid-gas universality class, was observed for finite systems inside the coexistence region [203]. Moreover a good quality scaling of the cluster size distribution was obtained using the Fisher's formula for the scaling function at subcritical as well as supercritical densities with values for the critical exponents compatible (within finite size effects) with the universality class of the model [268]. This indicates that the observation of scaling does not allow to infer the position of the critical zone as it is also compatible with a fragmentation inside the coexistence region of a first order phase transition. Concerning the order parameter fluctuations, simulations have been performed in the framework of the Ising model [273] which

show that the distribution of the heaviest fragment approximately obeys the $\Delta=1$ scaling regime even at subcritical densities where no continuous transition takes place. The observed behaviour was interpreted as a finite size effect that prevents the recognition of the order of a transition in a small system. More recently the distribution of the heaviest fragment was analyzed within the lattice gas model [225] and it was shown that the most important finite size effect comes from conservation laws, the distribution of the order parameter being strongly deformed if a constraint is applied (mass conservation) to an observable that is closely correlated to the order parameter. Moreover the observation of the $\Delta=1$ scaling regime was indeed observed in the critical zone but was also confirmed at subcritical densities inside the coexistence region.

Very recently a generalization of Fisher's model to extend and quantify finite size effects was also proposed [226]. The Fisher's formula along the coexistence line is modified to the case of a vapor in equilibrium with a finite liquid drop replacing the original formula by $dN/dA = \eta(A) = q_0[A(A_d - A)/A]^{-\tau} \exp((-c_0(T)\varepsilon)/T[A^\sigma + (A_d - A)^\sigma - A_d^\sigma])$.

Such a generalization was tested within the canonical lattice gas model. Better results are obtained for $d=2$ (square lattice) than for $d=3$ (cubic lattice). Applications to experimental data are needed to evaluate that potential improvement. To conclude that part one can say that, from both experiments and theory, many different pseudo-critical behaviours can be observed inside the coexistence region of a first-order phase transition as far as finite systems are concerned.

9 Coherent experimental signals of phase transition

As shown in the previous sections, signals of phase transitions were observed by many experimental groups for systems with different sizes and excitation energies. In most cases however only one signal was evidenced, which is not sufficient to convince that a phase transition does occur, because each of the proposed signals has some intrinsic weakness. The quality of the exclusive measurements nowadays permits to search for several different signatures of the transition on a given sample of events; indeed the concomitant observation of several signals strongly reinforces the hypothesis that a phase transition has occurred. Several groups are presently looking for different signals in their samples. For instance, and if we restrict to reactions below 100 MeV/nucleon, the group of Bologna studied QPs from Au+Au collisions at 35 MeV/nucleon, and after having discovered the negative branch of the heat capacity [245], they showed also Fisher scaling, critical exponents [266] and more recently they examine the possible occurrence of a bimodal distribution (see below) of the charge of the largest fragment [274]. The INDRA collaboration evidenced several signatures of phase transition for Au QPs, and for central collisions

between Ni and Ni, Ni and Au, Xe and Sn (see ref [237, 248, 267]. A rather good coherence of the different signatures was found in these cases. We chose to focus in this section on three sets of data for which the most extended analyses were realized. They cover different system sizes and collision centrality. The findings will only be summarized, the reader is sent to the quoted references for details:

- 1) light quasi-projectiles ($A \sim 36$), from reactions between 47 MeV/nucleon ^{40}Ar and ^{27}Al , ^{48}Ti and ^{58}Ni , by Ma *et al* [42];
- 2) heavy quasi-projectiles from Au on Au reactions, by the INDRA/ALADIN collaboration [74, 158, 275];
- 3) fused systems of mass around 200 formed in central collisions between Xe and Sn, by the INDRA collaboration [15, 72, 263, 264, 275].

Besides the signals mentioned in the previous section, Ma *et al* proposed some other ones as possible signatures of phase transition or critical behaviour, and firstly the nuclear Zipf law [276, and references therein]. Zipf law, first introduced in linguistic to analyse the relative population of words in English texts, says that the frequency of a word is inversely proportional to its rank, n , in a frequency list (the integer rank n is equal to 1 for the most frequently used word). It was afterwards evidenced in many different scientific areas and thus it was suggested that the Zipf hierarchy is a fingerprint of criticality. In nuclear physics, investigations with a lattice gas model showed that cluster distributions follow a Zipf law, where the frequency is replaced by the average size (charge or mass) of the clusters: $\langle Z_n \rangle \propto n^{-\lambda}$, where $n = 1, 2 \dots$ for the largest, second largest \dots fragment of each partition; λ was found equal to 1 (the Zipf law is verified) at the phase transition temperature. Ma fitted the average values of the charges of the multifragmentation clusters (starting at $Z=1$) as a function of their rank with this type of law for different excitation energies: λ is found to decrease with increasing energy. The Zipf law is verified ($\lambda = 1$) for the energy bin 5-6 MeV/nucleon. Consistently with the formulation of the Zipf law, percolation models suggest that the ratio of the sizes of the second to the first largest fragments, $S_p = \langle Z_{max2} \rangle / \langle Z_{max} \rangle$, takes the value 0.5 around the phase separation point [277]. And indeed, in the sample studied by Ma, S_p exhibits essentially linear behaviours, with a change of slope around the energy of 5.2 MeV/nucleon, where it takes the value of 0.5.

As mentioned in section 8, for finite systems, in the transition zone of a first order phase transition, the distribution of the order parameter presents a bimodal behaviour in the canonical ensemble, due to an anomalous convexity in the underlying microcanonical entropy. The transition energy, $E_{tr}^{bimodality}$, corresponds to the value for which the two bumps of the bimodal distribution have the same height. In the case of multifragmentation, the size of the heaviest cluster, which is correlated with the total energy deposit and the system density/volume, appears as a natural potential order parameter (see also the universal scaling laws in sect. 8.3.2). The bimodal character of the

distribution may however be hidden if the variable is constrained by a conservation law. Bimodality was searched for by using different observables connected with the charge partition of the events; the chosen variable in cases 1) and 3), where a limited excitation energy range was covered, has the form: $P_b = (\sum_{Z_i \geq Z_{lim}} Z_i - \sum_{Z_i < Z_{lim}} Z_i) / \sum_{Z_i \geq Z_{th}}$, with Z_{lim} and Z_{th} equal to 4 and 1 for case 1), and 13 and 3 for case 3). P_b can be viewed as the difference between the liquid and the gas densities. In case 2) the distribution studied was firstly that of the asymmetry between the two largest fragments [158], $(Z_{max} - Z_{max2}) / (Z_{max} + Z_{max2})$; in a second step an elaborated analysis was performed, which consisted in weighting the Z_{max} distribution by a probability given by the correlated excitation energy distribution on the total range scanned [74, 242].

The signals studied for the three systems investigated, and the excitation energy at which they occur are listed in table 1; these energies are those coming from the calorimetry performed, and may thus include not only thermal energy but also some collective component. Scalings, fluctuations of the configurational energy and of the largest fragment charge, sudden changes in the evolution of key variables, topological structure of the fragment partitions, charge correlations were examined.

- (1) For the light $A \sim 36$ system, in the Texas A&M experiment, both charged products and neutrons were measured and used for centrality selections. A completeness criterion ($Z_{QP} \geq 12$) was applied, and QP formed in *central collisions* were analysed. The QP excitation energy, derived by calorimetry, ranges between 2 and 10 MeV/nucleon with a mean value around 4.5 MeV/nucleon. Such a distribution does clearly not reflect the expected impact parameter dependence, meaning that at low energy all the possible QP partitions are not explored. In this context, all the variables characterizing a phase transition studied present a coherent behaviour, with a change in their evolution in the range 5-6 MeV/nucleon. Note however that, while a maximum of the configurational energy fluctuations is observed, its value remains very low (0.3), far below the canonical expectation of 3/2. The authors give thus no firm statement about the observation of a negative heat capacity. Their global conclusion is that they show a body of evidence suggesting a liquid-gas phase change in an equilibrated system at, or extremely close to, the critical point.
- (2) For Au quasi-projectiles a completeness criterion is also required and calorimetry measurements lead to an excitation energy distribution decreasing from 2 to 11 MeV/nucleon. For these heavier QP, with a charge ~ 68 , a similar consistency between all the signals of phase transition emerges. The maxima of fluctuations (fig. 42) and E_{crit}^{Fisher} are in the range 4-5 MeV/nucleon, well inside the domain where the heat capacity is negative. The changes in the fragment topology (inversion of variation of $\langle Z_{max2} \rangle$, $E_{tr}^{bimodality}$) occur near the second divergence of the

Table 1

Excitation energies - in MeV/nucleon - at which different signals were observed for three systems (see text). The energy values were derived from calorimetry. Z_s is the charge of the considered source. E_{crit}^{Fisher} is the excitation energy corresponding to T_c in Fisher formula (see sect. 8 and see text for the other definitions of variables). The threshold for radial expansion energy is reported for information (see sect. 4)

variable	QP $A_s \sim 36$	QP $Z_s \sim 68$	monosources $Z_s \sim 82$
E_{crit}^{Fisher}	5-6	4.2	3.8-4.5
Δ scaling	5-6	-	6.2
$\max A_s \sigma_k^2 / T^2$	4-6.5	4-5	≤ 4
$\max \sigma_{Z_{max}}^2 / \langle Z_{max} \rangle$	5-6	-	-
$c < 0$	-	[2.5:5.5]	[-:6.5]
$\max \sigma_{Z_{max}} / Z_s$	-	4-5	≤ 5
$\max \langle Z_{max2} \rangle$	6	5	4.5-6
$E_{Zipf}: \lambda = 1$	5.6	8.5	7.5
$S_p = 0.5$	5.2	8.5 and above	3.2 - 6
change slope S_p	5.6	4	-
$E_{tr}^{bimodality}$	5.6	[4.75:5.25]	7.8
spinodal	-	[5:8]	[5:9]
threshold ε_{rad}	-	$\sim 5.$	~ 4.5

heat capacity, located at ~ 5 MeV/nucleon, as does the maximum of the extra equal-sized fragment events, possible witnesses of a spinodal decomposition. The values of E_{crit}^{Fisher} and the position of the energies at which the heat capacity diverges agree within 10% with those obtained from another sample of events obtained with the Multics/Miniball device [245, 266]. Conversely, while the variable S_p changes slope in the same domain, it reaches a value of 0.5 - where it saturates - at a much higher energy (8.5 MeV/nucleon, see fig. 43); consistently the Zipf law is verified at the same high value (only fragments with $Z \geq 3$ were taken into account for the heavy systems). In that case, the observations plead in favor of the occurrence of a first order phase transition of the liquid-gas type. The transition energy is lower than that derived for the lighter QP; the Zipf law and related signals can not be taken as a sign of transition.

- (3) What can be said for the monosources formed in central Xe+Sn collisions at 25, 32, 39, 45 and 50 MeV/nucleon, which are slightly heavier than the QP of case 2)? They were isolated by a detected-charge completeness criterion, and by selecting events with a flow angle greater than 60° (compact event shapes in velocity space). The average excitation energies determined by calorimetry lie between ~ 5 and ~ 10 MeV/nucleon. In agree-

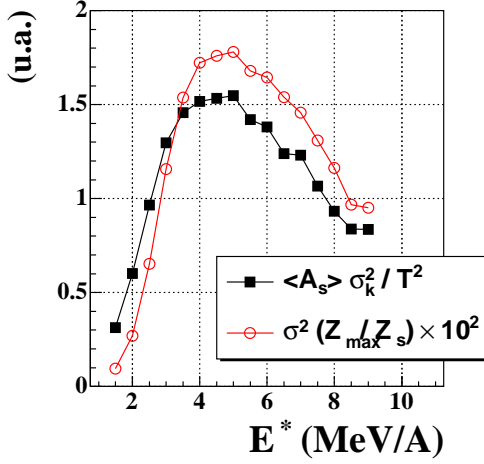


Fig. 42. Normalized fluctuations as a function of the excitation energy for Au QP (Au + Au 80 MeV/nucleon). Open circles correspond to fluctuations of the largest fragment normalized by the source size Z_1/Z_s and full squares refer to normalized configurational energy fluctuations. (from [278]).

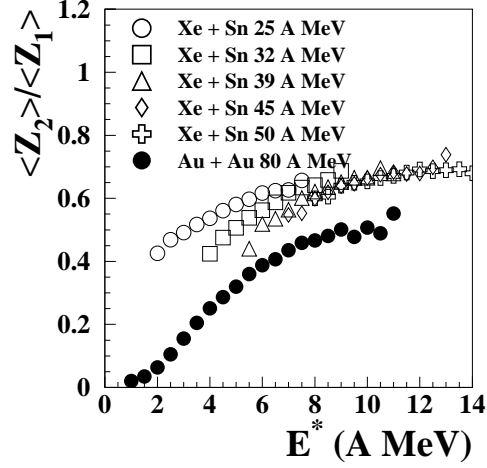


Fig. 43. Evolution of the variable S_p versus the excitation energy for Au quasi-projectiles and Xe+Sn compact sources from central collisions. data are from the INDRA collaboration.

ment with the previous case, the fluctuations of both the configurational energy and the largest fragment charge, and the average charge of the second largest fragment, present a maximum in the region 4-5 MeV/nucleon where lies also E_{crit}^{Fisher} . Only the second divergence of the heat capacity is seen in the explored energy range, at a slightly higher than for Au QP's. The change of Δ scaling and the maximum of extra equal-sized fragment events occur near the second divergence, while the transition energy indicated by the bimodality signal is slightly higher (however the answer in that case is somewhat dependent on the chosen value of Z_{lim}). Note that the Z_{max} distributions are never bimodal in monosources, due to the strong constraints on the energy. Finally the Zipf law is also verified above the second divergence, while the variable S_p takes the value of 0.5 inside the coexistence region, but at an excitation energy varying with the incident energy (fig 43). Let us underline that monosources with close mass and charge were also formed with an asymmetric entrance channel, Ni+Au, and that negative heat capacities and signal of spinodal decomposition were observed in an energy range consistent with that quoted for Xe+Sn [237].

The consistency of all signals for central collisions is however not as good as in the Au QP case. It must be noted that for QP's radial expansion energy appears just above the higher limit of the coexistence region. Conversely the threshold of expansion lies inside the coexistence region for

the monosources and may have a different influence on the signals, particularly those related to the fragment topology: indeed as explained in sect. 8, radial expansion prevents coalescence between the nascent fragments, favouring the observation of the spinodal signal.

In conclusion of this section, it may be said that a large body of signals of phase transition has been obtained in the three cases examined here. The transition energy is higher when the system is lighter. The radial energy seems to influence the energy at which some signals occur, leading to a better overall consistency for QP's than for monosources formed in violent collisions. Finally there is no indication that the Zipf law is a signal of phase transition or critical behaviour for the two heavy systems studied by the INDRA collaboration. The excitation energy, E_{Zipf} , at which the Zipf law is verified was however shown to vary with the minimal value of the charge of the considered fragments: raising this value shifts E_{Zipf} downwards [275]. One may thus suspect a connection between the system size and the range of charge to consider in order to establish the Zipf law. While Ma *et al.* conclude that “the transition occurs close to the critical point” for their light system, for heavy systems the ensemble of results inclines towards the occurrence of a first order phase transition.

10 Conclusions

With the advent of powerful multidetectors dedicated to the study of multifragmentation, which allow in particular the detection of more complete events, important improvements have been realized in the sorting of data and the construction of global observables. New correlation methods were developed (higher order charge correlations, fragment-particle) to investigate fragment formation mechanism and primary fragment excitation energy. Yield scaling as well as various fluctuation properties were also studied in relation with phase transition. Detailed and instructive comparisons with dynamical and statistical models have been reported.

Fragment emission exhibits both dynamical and statistical aspects. For example, heavy-ion collisions and hadron-nucleus collisions were used to clearly show that fragment radial expansion energy is higher for central heavy-ion collisions for which a compression-expansion phase is predicted to occur in dynamical simulations; deduced radial expansion energies from experiments are around 4-5 MeV/nucleon at the maximum of fragment production. Fragment multiplicity appears as mainly governed by thermal energy whereas fragment partitions seem to be sensitive to radial expansion, which could be an indication of different trajectories in the phase diagram. Note that statistical models predict the sensitivity of partitions to break-up density/volume. Fragment-particle correlation studies strongly suggest that primary fragments

are, on average, in thermal equilibrium. That result is supported by both the success of statistical models in describing rather well average multifragmentation properties and the information derived from dynamical simulations concerning the different time scales involved along the collisions. A saturation of the average excitation energy of primary fragments around 3 MeV/nucleon is also deduced. Moreover a few recent examples show a rather coherent link between dynamical and statistical descriptions.

What is the mechanism of fragment formation? It is still an open question. In stochastic mean field approaches the fragmentation process follows the spinodal decomposition scenario whereas in molecular dynamics many-body correlations play a stronger role and pre-fragments appear at earlier times. New experiments with larger statistics are needed to eventually demonstrate through fragment charge correlations that spinodal instabilities could be responsible of fragmentation. On the theoretical side, although large progresses have been made, the development of quantal transport theory is still a challenge to formally describe the basic quantal nature of hot nuclear systems and of their fragmentation.

The specific role of the largest fragment in each event was also clearly revealed. Firstly, at a given excitation energy, its charge distribution is independent of the total mass of the multifragmenting system when the latter exceeds $A \sim 180-190$; this behaviour is also observed in statistical models down to $A \sim 150$. Then, its specific position close to the centre of mass of the multifragmenting systems produced in central heavy-ion collisions, and more randomly positioned for ^3He -nucleus collisions, informs on event topology at freeze-out. Finally, its scaling properties and bimodal distributions can indicate that the largest fragment may be considered as a good candidate as order parameter of a phase transition in nuclei.

Since the early eighties multifragmentation has been tentatively associated with the liquid-gas phase transition theoretically predicted for nuclear matter at sub-saturation densities and temperature below 16-18 MeV. However, when dealing with the breaking of a nucleus, statistical mechanics of finite systems appeared as a key issue to progress and propose new first-order phase transition signatures related to thermodynamic anomalies like negative micro-canonical heat capacity and bimodalities. Those anomalies are generic features in non-extensive systems and have been reported in other fields such as atomic cluster physics and self-gravitating systems.

A big effort to accumulate experimental indications of a phase transition has been presently made, including scaling and fluctuations for fragment sizes. At the same time progresses have been obtained to experimentally better localize nuclear multifragmentation in the nuclear phase diagram thanks to improvements in calorimetry, thermometry and estimates of density at the break-up stage within working hypotheses and approximations. Today a rather coherent picture has been reached for few exhaustive studies and some semi-quantitative estimates of the transition region become available. However the order and the

nature of the transition is still subject to debate. For a large part this debate is related to finite-size effects, which remain an important challenge.

How to progress further ? Experimentally new advances can be made *by identifying charge but also mass of fragments with the construction of a new generation of 4π multidetectors*. With such new devices some hypotheses would be reduced or suppressed to evaluate freeze-out properties from intra-event correlations and it would become possible to disentangle radial expansion from Coulomb repulsion. On the theoretical side, by largely varying the proportions of neutrons and protons, a new phenomenon related to the phase transition for nuclei is predicted: the distillation, which makes the gas phase more asymmetric than the liquid phase (even more asymmetric for spinodal decomposition as compared to phase equilibrium). By measuring the isotopic composition of all the fragments it would become possible to identify the two phases and determine by a new way the dynamics of the transition.

References

- [1] N. Bohr, Nature 137 (1936) 351.
- [2] R. T. de Souza et al., P. Chomaz et al. (eds.) Dynamics and Thermodynamics with nuclear degrees of freedom, Springer, 2006, vol. 30 of *Eur. Phys. J. A*, 275–291.
- [3] C. Fuchs et al., P. Chomaz et al. (eds.) Dynamics and Thermodynamics with nuclear degrees of freedom, Springer, 2006, vol. 30 of *Eur. Phys. J. A*, 5–22.
- [4] A. Ono et al., P. Chomaz et al. (eds.) Dynamics and Thermodynamics with nuclear degrees of freedom, Springer, 2006, vol. 30 of *Eur. Phys. J. A*, 109–120.
- [5] P. J. Siemens, Nature 305 (1983) 410.
- [6] K. A. Bugaev et al., Phys. Rev. C 62 (2000) 044320.
- [7] K. A. Bugaev et al., Phys. Lett. B 498 (2001) 144.
- [8] H. Jaquaman et al., Phys. Rev. C 27 (1983) 2782.
- [9] H. R. Jaquaman et al., Phys. Rev. C 29 (1984) 2067.
- [10] L. P. Csernai et al., Phys. Rep. 131 (1986) 223.
- [11] H. Müller et al., Phys. Rev. C 52 (1995) 2072.
- [12] G. F. Bertsch et al., Phys. Lett. B 126 (1983) 9.
- [13] H. Heiselberg et al., Phys. Rev. Lett. 61 (1988) 818.
- [14] J. López et al., Phys. Lett. B 219 (1989) 215.
- [15] B. Borderie, J. Phys. G: Nucl. Part. Phys. 28 (2002) R217.
- [16] J. N. De et al., Phys. Rev. C 59 (1999) 1.
- [17] A. J. Cole, Statistical Models for Nuclear Decay, Institute of Physics Publishing, Bristol, 2000.
- [18] L. Beaulieu et al., Phys. Rev. C 54 (1996) 973.
- [19] A. Schuttauf et al. (ALADIN Collaboration), Nucl. Phys. A 607 (1996) 457.
- [20] N. Le Neindre, thèse de doctorat, Université de Caen (1999), <http://tel.archives-ouvertes.fr/tel-00003741>.
- [21] N. Bellaize et al. (INDRA Collaboration), Nucl. Phys. A 709 (2002) 367.
- [22] R. J. Charity et al., Nucl. Phys. A 511 (1990) 59.
- [23] R. Bougault et al., Phys. Lett. B 232 (1989) 291.
- [24] M. Louvel et al., Phys. Lett. B 320 (1994) 221.
- [25] M. Louvel et al., preprint LPCC 95-01 (1995).
- [26] C. J. Gelderloos et al., Phys. Rev. Lett. 75 (1995) 3082.
- [27] Z. Y. He et al., Phys. Rev. C 63 (2000) 011601.
- [28] Z. Y. He et al., Phys. Rev. C 65 (2001) 014606.
- [29] L. Beaulieu et al., Phys. Rev. C 64 (2001) 064604.
- [30] V. A. Karnaukhov, Phys. of Particles and Nuclei. 37 (2006) 165.
- [31] M. B. Tsang et al., Phys. Rev. Lett. 71 (1993) 1502.
- [32] C. O. Bacri et al. (INDRA Collaboration), Phys. Lett. B 353 (1995) 27.
- [33] M. F. Rivet et al. (INDRA Collaboration), Phys. Lett. B 388 (1996) 219.
- [34] B. Borderie et al. (INDRA Collaboration), Phys. Lett. B 388 (1996) 224.
- [35] L. Pienkowski et al., Phys. Lett. B 472 (2000) 15.

- [36] B. Borderie et al. (INDRA Collaboration), *Eur. Phys. J. A* 6 (1999) 197.
- [37] F. Gulminelli et al., *Nucl. Phys. A* 615 (1997) 117.
- [38] P. Lantesse et al. (INDRA Collaboration), *Eur. Phys. J A* 27 (2006) 349.
- [39] W. Gawlikowicz et al., *Prog. Rep.* DE/ER/40414-18 (2005), <http://nuchem.chem.rochester.edu/webreports.html>.
- [40] D. R. Bowman et al., *Phys. Rev. C* 67 (1991) 1527.
- [41] J. Töke et al., *Phys. Rev. C* 63 (2001) 024604.
- [42] Y. G. Ma et al., *Phys. Rev. C* 71 (2005) 054606.
- [43] P. Kreuzt et al., *Nucl. Phys. A* 556 (1993) 672.
- [44] D. Doré et al. (INDRA Collaboration), *Phys. Rev. C* 63 (2001) 034612.
- [45] E. Galichet et al. (2007), to be published.
- [46] L. G. Moretto et al., *Phys. Rep* 287 (1997) 249.
- [47] J. Lukasik et al. (INDRA Collaboration), *Phys. Rev. C* 55 (1997) 1906.
- [48] B. Jouault et al., *Nucl. Phys. A* 628 (1998) 119.
- [49] R. Yanez et al., *Phys. Rev C* 68 (2003) 011602.
- [50] S. Piantelli et al., *Phys. Rev. C* 74 (2006) 034609.
- [51] V. Baran et al., *Nucl. Phys. A* 703 (2002) 603.
- [52] W. J. Llope et al., *Phys. Rev. C* 51 (1995) 1325.
- [53] M. Colonna et al., *Nucl. Phys. A* 642 (1998) 449.
- [54] G. Buchwald et al., *Phys. Rev. Lett.* 52 (1984) 1594.
- [55] W. Schmidt et al., *Phys. Rev. C* 47 (1993) 2782.
- [56] B. Kämpfer et al., *Phys. Rev. C* 48 (1993) 955.
- [57] J. F. Lecomte et al. (INDRA Collaboration), *Nucl. Instr. and Meth. in Phys. Res. A* 441 (2000) 517.
- [58] P. Désesquelles, *Ann. Phys. Fr.* 20 (1995) 1.
- [59] P. Désesquelles et al., *Phys. Rev. C* 53 (1996) 2252.
- [60] C. David et al., *Phys. Rev. C* 51 (1995) 1453.
- [61] S. A. Bass et al., *Phys. Rev. C* 53 (1996) 2358.
- [62] F. Haddad et al., *Phys. Rev. C* 55 (1997) 1371.
- [63] P. Désesquelles et al. (INDRA Collaboration), *Phys. Rev. C* 62 (2000) 024614.
- [64] P. Lantesse et al. (INDRA Collaboration), *Phys. Rev. C* 71 (2005) 034602.
- [65] R. Moustabchir, thèse de doctorat, Université Claude Bernard - Lyon I et Université Laval Québec (2004), <http://tel.archives-ouvertes.fr/tel-00008654>.
- [66] P. Lantesse, Habilitation à diriger des recherches, Université Claude Bernard Lyon (2005), <http://tel.archives-ouvertes.fr/tel-00127989>.
- [67] C. Cavata et al., *Phys. Rev. C* 42 (1990) 1760.
- [68] C. A. Ogilvie et al., *Phys. Rev. Lett.* 67 (1991) 1214.
- [69] D. Sisan et al., *Phys. Rev. C* 63 (2001) 027602.
- [70] A. Insolia et al. (EOS Collaboration), *Phys. Rev. C* 61 (2000) 044902.
- [71] W. Reisdorf et al. (FOPI Collaboration), *Phys. Lett. B* 595 (2004) 118.
- [72] G. Tăbăcaru et al., *Eur. Phys. J. A* 18 (2003) 103.
- [73] G. F. Peaslee et al., *Phys. Rev. C* 49 (1994) 2271.
- [74] E. Bonnet, thèse de doctorat, Université Paris-XI Orsay (2006), <http://tel.archives-ouvertes.fr/tel-00121736>.
- [75] B. Tamain, P. Chomaz et al. (eds.) *Dynamics and Thermodynamics with nuclear degrees of freedom*, Springer, 2006, vol. 30 of *Eur. Phys. J. A*, 71–79.
- [76] M. F. Rivet et al. (INDRA Collaboration), *Phys. Lett. B* 430 (1998) 217.
- [77] S. Hudan, thèse de doctorat, Université de Caen (2001), GANIL T 01 07.
- [78] G. Tăbăcaru et al. (INDRA Collaboration), *Nucl. Phys. A* 764 (2006) 371.
- [79] V. E. Viola et al., *Phys. Rev. Lett.* 93 (2004) 132701.
- [80] A. R. Raduta et al., *Phys. Lett. B* 623 (2005) 43.
- [81] R. Wada et al. (NIMROD Collaboration), *Phys. Rev. C* 69 (2004) 044610.
- [82] F. Lavaud, thèse de doctorat, Université Louis Pasteur Strasbourg I (2001), <http://tel.archives-ouvertes.fr/tel-00004100>.
- [83] B. Bouriquet, thèse de doctorat, Université de Caen (2001), <http://tel.archives-ouvertes.fr/tel-00003803>.
- [84] R. Pak et al., *Phys. Rev. C* 54 (1996) 1681.
- [85] C. Williams et al., *Phys. Rev. C* 55 (1997) 2132.
- [86] M. D'Agostino et al., *Phys. Lett. B* 371 (1996) 175.
- [87] D. Durand et al., Preprint LPCC 96-02 (1996).
- [88] B. Borderie, G. Giardina et al. (eds.) *Proc. Int. Symposium on large-scale collective motions of atomic nuclei*, Brolo, Italy, World scientific, 1997, 1.
- [89] W. Reisdorf et al., *Ann. Rev. Nucl. Part. Sci.* 47 (1997) 663.
- [90] Anh-Dung Nguyen, thèse de doctorat, Université de Caen (1998), LPCC T 98-02.
- [91] J. D. Frankland et al. (INDRA Collaboration), *Nucl. Phys. A* 689 (2001) 940.
- [92] A. Le Fèvre et al. (INDRA and ALADIN collaborations), *Nucl. Phys. A* 735 (2004) 219.
- [93] C. B. Das et al., *Phys. Rev. C* 70 (2004) 064610.
- [94] F. Gulminelli et al., *Nucl. Phys. A* 734 (2004) 581.
- [95] S. Salou, thèse de doctorat, Université de Caen (1997), <http://tel.archives-ouvertes.fr/tel-00003688>.

- [96] S. C. Jeong et al., Nucl. Phys. A 604 (1996) 208.
- [97] M. D'Agostino et al., Nucl. Phys. A 650 (1999) 329.
- [98] L. Beaulieu et al. (ISIS Collaboration), Phys. Rev. Lett. 84 (2000) 5971.
- [99] A. Le Fèvre, thèse de doctorat, Université Paris 7 - Denis Diderot (1997), GANIL T 97 03.
- [100] P. Désesquelles et al. (Multics/Miniball Collaboration), Nucl. Phys. A 633 (1998) 547.
- [101] N. Marie et al. (INDRA Collaboration), Phys. Lett. B 391 (1997) 15.
- [102] A. Z. Mekjian, Phys. Rev. C 17 (1978) 1051.
- [103] G. Fáí et al., Nucl. Phys. A 404 (1983) 551.
- [104] S. E. Koonin et al., Nucl. Phys. A 474 (1987) 173.
- [105] D. H. E. Gross, Rep. Prog. Phys. 53 (1990) 605.
- [106] S. J. Lee et al., Phys. Rev. C 45 (1992) 1284.
- [107] D. Hahn et al., Phys. Rev. C 37 (1988) 1048.
- [108] D. Hahn et al., Nucl. Phys. A 476 (1988) 718.
- [109] J. Konopka et al., Phys. Rev. C 50 (1994) 2085.
- [110] J. Bondorf et al., Phys. Rep. 257 (1995) 133.
- [111] A. H. Raduta et al., Phys. Rev. C 55 (1997) 1344.
- [112] A. H. Raduta et al., Phys. Rev. C 61 (2000) 034611.
- [113] G. Peilert et al., Phys. Rev. C 39 (1989) 1402.
- [114] J. Aichelin, Phys. Rep. 202 (1991) 233.
- [115] J. Łukasik et al., Acta Phys. Polonica B 24 (1993) 1959.
- [116] A. Ono et al., Phys. Rev. C 47 (1993) 2652.
- [117] H. Feldmeier, Nucl. Phys. A 515 (1990) 147.
- [118] A. Ono et al., Phys. Rev. C 53 (1996) 2598.
- [119] Y. Sugawa et al., Phys. Rev. C 60 (1999) 064607.
- [120] R. Nebauer et al. (INDRA Collaboration), Nucl. Phys. A 658 (1999) 67.
- [121] S. Pratt et al., Phys. Lett. B 349 (1995) 261.
- [122] S. Ayik et al., Phys. Lett. B 212 (1988) 269.
- [123] S. Ayik et al., Nucl. Phys. A 513 (1990) 187.
- [124] J. Randrup et al., Nucl. Phys. A 514 (1990) 339.
- [125] P. Chomaz et al., Phys. Lett. B 254 (1991) 340.
- [126] P. Reinhard et al., Ann. Phys. 213 (1992) 204.
- [127] P. Reinhard et al., Ann. Phys. 216 (1992) 98.
- [128] P. Reinhard et al., Nucl. Phys. A 545 (1992) 59c.
- [129] P. Chomaz et al., Phys. Rev. Lett. 73 (1994) 3512.
- [130] A. Guarnera et al., Phys. Lett. B 373 (1996) 267.
- [131] A. Guarnera et al., Phys. Lett. B 403 (1997) 191.
- [132] P. Chomaz, Ann. Phys. Fr. 21 (1996) 669.
- [133] F. Matera et al., Phys. Rev. C 62 (2000) 044611.
- [134] S. J. Lee et al., Phys. Rev. C 56 (1997) 2621.
- [135] A. S. Parvan et al., Nucl. Phys. A 676 (2000) 409.
- [136] C. B. Das et al., Phys. Rev. C 64 (2001) 017601.
- [137] P. Chomaz et al., Phys. Rev. Lett. 85 (2000) 3587.
- [138] W. A. Friedman, Phys. Rev. C 42 (1990) 667.
- [139] D. R. Bowman et al., Phys. Rev. C 52 (1995) 818.
- [140] R. J. Charity et al., Nucl. Phys. A 483 (1988) 371.
- [141] R. P. Scharenberg et al. (EOS Collaboration), Phys. Rev. C 64 (2001) 054602.
- [142] B. K. Srivastava et al. ((EOS Collaboration)), Phys. Rev. C 65 (2002) 054617.
- [143] K. Zbiri et al. (ALADIN and INDRA collaborations), Phys. Rev. C 75 (2007) 034612.
- [144] H. Kruse et al., Phys. Rev. C 31 (1985) 1770.
- [145] C. Grégoire et al., Nucl. Phys. A 465 (1987) 317.
- [146] G. F. Bertsch et al., Phys. Rep. 160 (1988) 189.
- [147] A. Bonasera et al., Phys. Rep. 243 (1994) 1.
- [148] A. Strachan et al., Phys. Rev. C 59 (1999) 285.
- [149] D. Cussol, Phys. Rev. C 65 (2002) 054614.
- [150] A. Chermomoretz et al., Phys. Rev. C 69 (2004) 034610.
- [151] W. Müller et al., Phys. Lett. B 298 (1993) 27.
- [152] A. Ono, Phys. Rev. C 59 (1999) 853.
- [153] S. Ayik et al., Phys. Rev. C 50 (1994) 2947.
- [154] G. Tăbăcaru, thèse de doctorat, Université Paris-XI Orsay (2000), <http://tel.archives-ouvertes.fr/tel-00007912>.
- [155] A. H. Raduta et al., Phys. Rev. C 74 (2006) 034604.
- [156] A. Lleres et al., Phys. Rev. C 48 (1993) 2753.
- [157] R. Planeta et al., Eur. Phys. J. A 11 (2001) 297.
- [158] M. Pichon et al. (INDRA and ALADIN collaborations), Nucl. Phys. A 779 (2006) 267.
- [159] E. Vient, Habilitation à diriger des recherches, Université de Caen (2006), <http://tel.archives-ouvertes.fr/tel-00141924>.
- [160] J. A. Hauger et al. (EOS Collaboration), Phys. Rev. Lett. 77 (1996) 235.
- [161] V. E. Viola et al., Phys. Rep. 434 (2006) 1.

- [162] M. Jandel et al., *J. Phys. G: Nuclear and Particle Physics* 31 (2005) 29.
- [163] S. Hudan et al., *Phys. Rev. C* 71 (2005) 054604.
- [164] K. Stimmerer et al., *Phys. Rev. C* 61 (2000) 034607.
- [165] R. J. Charity, *Phys. Rev. C* 58 (1998) 1073.
- [166] T. Lefort et al., *Phys. Rev. C* 64 (2001) 064603.
- [167] J. C. Steckmeyer et al. (INDRA Collaboration), *Nucl. Phys. A* 686 (2001) 537.
- [168] S. Das Gupta et al., *Adv. Nucl. Phys.* 26 (2001) 91.
- [169] A. Kelić et al., P. Chomaz et al. (eds.) *Dynamics and Thermodynamics with nuclear degrees of freedom*, Springer, 2006, vol. 30 of *Eur. Phys. J. A*, 203–213.
- [170] M. Gonin et al., *Phys. Rev. C* 42 (1990) 2125.
- [171] R. Ortega et al., *Eur. Phys. J. A* 28 (2006) 161.
- [172] S. Albergo et al., *Nuovo Cimento* 89 A (1985) 1.
- [173] A. H. Raduta et al., *Phys. Rev. C* 59 (1999) 1855.
- [174] M. B. Tsang et al., *Phys. Rev. Lett.* 78 (1997) 3836.
- [175] A. H. Raduta et al., *Nucl. Phys. A* 671 (2000) 600.
- [176] K. H. Schmidt et al., *Nucl. Phys. A* 710 (2002) 157.
- [177] J. B. Natowitz et al., *Phys. Rev. C* 65 (2002) 034618.
- [178] J. Pochodzalla et al. (ALADIN Collaboration), *Phys. Rev. Lett.* 75 (1995) 1040.
- [179] P. Bonche et al., *Nucl. Phys. A* 427 (1984) 278.
- [180] P. Bonche et al., *Nucl. Phys. A* 436 (1986) 265.
- [181] D. G. d’Enterria et al., *Phys. Lett. B* 538 (2002) 27.
- [182] M. Pârlog et al., *Eur. Phys. J. A* 25 (2005) 223.
- [183] Y. D. Kim et al., *Phys. Rev. C* 45 (1992) 387.
- [184] W. A. Zajc et al., *Phys. Rev. C* 29 (1984) 2173.
- [185] M. A. Lisa et al., *Phys. Rev. C* 44 (1991) 2865.
- [186] D. Fox et al., *Phys. Rev. C* 47 (1993) 421.
- [187] E. Bauge et al., *Phys. Rev. Lett.* 70 (1993) 3705.
- [188] D. R. Bowman et al., *Phys. Rev. Lett.* 70 (1993) 3534.
- [189] Zhi-Yong He et al., *Phys. Rev. C* 63 (2000) 011601.
- [190] T. C. Sangster et al., *Phys. Rev. C* 51 (1995) 1280.
- [191] G. Wang et al., *Phys. Rev. C* 60 (1999) 014603.
- [192] N. Marie et al. (INDRA Collaboration), *Phys. Rev. C* 58 (1998) 256.
- [193] S. Hudan et al. (INDRA Collaboration), *Phys. Rev. C* 67 (2003) 064613.
- [194] P. Staszal et al., *Phys. Rev. C* 63 (2001) 064610.
- [195] S. Fritz et al., *Phys. Lett. B* 461 (1999) 315.
- [196] J. B. Natowitz et al., *Phys. Rev. C* 66 (2002) 031601.
- [197] J. D. Frankland et al. (INDRA Collaboration), *Nucl. Phys. A* 689 (2001) 905.
- [198] S. Piantelli et al. (INDRA Collaboration), *Phys. Lett. B* 627 (2005) 18.
- [199] A. R. Raduta et al., *Phys. Rev. C* 72 (2005) 057603.
- [200] D. H. E. Gross, *Microcanonical Thermodynamics - Phase Transitions in “small” systems*, World Scientific, Singapore, 2001.
- [201] D. H. E. Gross et al., *Z. Phys. D* 35 (1995) 27.
- [202] D. H. E. Gross, *Phys. Rep.* 279 (1997) 119.
- [203] F. Gulminelli et al., *Phys. Rev. Lett.* 82 (1999) 1402.
- [204] P. Chomaz et al., *Nucl. Phys. A* 647 (1999) 153.
- [205] D. H. E. Gross et al., *Eur. Phys. J. B* 15 (2000) 115.
- [206] P. Borrmann et al., *Phys. Rev. Lett.* 84 (2000) 3511.
- [207] R. Botet et al., *Phys. Rev. E* 62 (2000) 1825.
- [208] J. Jellinek et al., *J. Chem. Phys.* 113 (2000) 2570.
- [209] O. Mülken et al., *Phys. Rev. C* 63 (2001) 024306.
- [210] X. Campi et al., *Nucl. Phys. A* 681 (2001) 458.
- [211] P. Chomaz et al., *Phys. Rev. E* 64 (2001) 046114.
- [212] J. M. Carmona et al., *Eur. Phys. J. A* 11 (2001) 87.
- [213] A. H. Raduta et al., *Phys. Rev. Lett.* 87 (2001) 202701.
- [214] A. H. Raduta et al., *Nucl. Phys. A* 703 (2002) 876.
- [215] L. G. Moretto et al., *Phys. Rev. C* 66 (2002) 041601.
- [216] F. Gulminelli et al., *Phys. Rev. C* 69 (2004) 069801.
- [217] A. H. Raduta et al., *Nucl. Phys. A* 724 (2003) 233.
- [218] P. Chomaz et al., *Physica A* 330 (2003) 451.
- [219] F. Gulminelli, *Ann. Phys. Fr.* 29 (2004) N° 6.
- [220] P. Chomaz et al., *Phys. Rep.* 389 (2004) 263.
- [221] L. G. Moretto et al., *Prog. Part. Nucl. Phys.* 53 (2004) 101.
- [222] C. B. Das et al., *Phys. Rep.* 406 (2005) 1.
- [223] X. Campi et al., *Phys. Rev. C* 71 (2005) 041601.
- [224] F. Gulminelli et al., *Phys. Rev. C* 72 (2005) 064618.
- [225] F. Gulminelli et al., *Phys. Rev. C* 71 (2005) 054607.
- [226] L. G. Moretto et al., *Phys. Rev. Lett.* 94 (2005) 202701.
- [227] J. N. De et al., *Phys. Rev. C* 73 (2006) 034602.

- [228] M. Colonna et al., Nucl. Phys. A 613 (1997) 165.
- [229] B. Jacquot et al., Phys. Lett. B 383 (1996) 247.
- [230] S. Ayik et al., Phys. Lett. B 353 (1995) 417.
- [231] D. Idier et al., Ann. Phys. Fr. 19 (1994) 159.
- [232] W. Nörenberg et al., Eur. Phys. J. A 9 (2000) 327.
- [233] B. Jacquot, thèse de doctorat, Université de Caen (1996), gANIL T 96 05.
- [234] M. Bruno et al., Phys. Lett. B 292 (1992) 251.
- [235] L. G. Moretto et al., Phys. Rev. Lett. 77 (1996) 2634.
- [236] J. L. Charvet et al., Nucl. Phys. A 730 (2004) 431.
- [237] B. Borderie et al., P. Chomaz et al. (eds.) Dynamics and Thermodynamics with nuclear degrees of freedom, Springer, 2006, vol. 30 of *Eur. Phys. J. A*, 243–251.
- [238] B. Borderie et al. (INDRA Collaboration), Phys. Rev. Lett. 86 (2001) 3252.
- [239] M. Colonna et al., Phys. Rev. Lett. 88 (2002) 122701.
- [240] W. Nörenberg et al., Eur. Phys. J. A 14 (2002) 43.
- [241] M. Challa et al., Phys. Rev. Lett. 60 (1988) 77.
- [242] F. Gulminelli, Nucl. Phys. A 791 (2007) 165.
- [243] F. Gulminelli et al., Europhys. Lett. 50 (2000) 434.
- [244] M. D’Agostino et al., Nucl. Phys. A 699 (2002) 795.
- [245] M. D’Agostino et al., Phys. Lett. B 473 (2000) 219.
- [246] N. Le Neindre et al. (INDRA collaboration), I. Iori et al. (eds.) Proc. XXXVIII Int. Winter Meeting on Nuclear Physics, Bormio, Italy, Ricerca scientifica ed educazione permanente, 2000, 404.
- [247] B. Guiot, thèse de doctorat, Université de Caen (2002), <http://tel.archives-ouvertes.fr/tel-00003753>.
- [248] B. Borderie et al., Nucl. Phys. A 734 (2004) 495.
- [249] M. D’Agostino et al., Nucl. Phys. 734 (2004) 512.
- [250] F. Gulminelli et al., P. Chomaz et al. (eds.) Dynamics and Thermodynamics with nuclear degrees of freedom, Springer, 2006, vol. 30 of *Eur. Phys. J. A*, 253–262.
- [251] N. Sator, Phys. Rep. 376 (2003) 1.
- [252] J. E. Finn et al., Phys. Rev. Lett. 49 (1982) 1321.
- [253] M. W. Curtin et al., Phys. Lett. 123 (1983) 289.
- [254] A. S. Hirsch et al., Phys. Rev. C 29 (1984) 508.
- [255] X. Campi et al., Phys. Lett. B 138 (1984) 353.
- [256] D. Stauffer et al., Introduction to Percolation Theory, Taylor & Francis Publishers, London, 1994.
- [257] X. Campi et al., Eur. Phys. J. D 11 (2000) 233.
- [258] M. Kleine Berkenbusch et al., Phys. Rev. Lett. 88 (2002) 022701.
- [259] M. E. Fisher, Physics 3 (1967) 255.
- [260] J. B. Elliott et al., Phys. Rev. Lett. 88 (2002) 042701.
- [261] J. B. Elliott et al., Phys. Rev. C 67 (2003) 024609.
- [262] R. Botet et al., Universal fluctuations, World Scientific, 2002, vol. 65 of *World scientific Lecture Notes in Physics*.
- [263] R. Botet et al., Phys. Rev. Lett. 86 (2001) 3514.
- [264] J. D. Frankland et al. (INDRA and ALADIN collaborations), Phys. Rev. C 71 (2005) 034607.
- [265] J. B. Elliott et al. (EOS Collaboration), Phys. Lett. B 418 (1998) 34.
- [266] M. D’Agostino et al., Nucl. Phys. 724 (2003) 455.
- [267] M. F. Rivet et al. (INDRA and ALADIN collaborations), Nucl. Phys. A 749 (2005) 73.
- [268] F. Gulminelli et al., Phys. Rev. C 65 (2002) 051601R.
- [269] C. B. Das et al., Phys. Rev. C 66 (2002) 044602.
- [270] J. B. Elliot et al., Phys. Rev. C 71 (2005) 024607.
- [271] L. G. Moretto et al., Phys. Rev. C 72 (2005) 064605.
- [272] E. J. Gumbel, Statistics of extremes, Columbia University Press, 1958.
- [273] J. M. Carmona et al., Phys. Lett. B 531 (2002) 71.
- [274] M. Bruno et al., Eur. Phys. J A (2007) submitted, [nucl-ex/0612030](http://arxiv.org/abs/nuc1-ex/0612030).
- [275] N. Le Neindre et al. (INDRA and ALADIN collaborations), Nucl. Phys. A 795 (2007) 44.
- [276] Y. G. Ma, Eur. Phys. J. A 6 (1999) 367.
- [277] A. J. Cole, Phys. Rev. C 65 (2002) 031601.
- [278] E. Bonnet et al. (INDRA and ALADIN collaborations), I. Iori et al. (eds.) Proc. XLV Int. Winter Meeting on Nuclear Physics, Bormio, Italy, Ricerca scientifica ed educazione permanente, 2007, hal.archives-ouvertes.fr/hal-00141043.